Theoretical assessments of Pd-PdO phase transformation and its impacts on H_2O_2 synthesis and decomposition pathways

Manasi Vyas, Fernando Fajardo-Rojas, Diego A Gómez-Gualdrón, Stephanie Kwon*
Department of Chemical and Biological Engineering, Colorado School of Mines, Golden, Colorado 80401, United States

** Corresponding author: kwon@mines.edu*

Keywords: Palladium, H_2O_2 synthesis, Pd-PdO transformation, density functional theory, ab-initio thermodynamics

Abstract

The direct synthesis of H_2O_2 from O_2 and H_2 provides a green pathway to produce H_2O_2, a popular industrial oxidant. Here, we theoretically investigate the effects of Pd oxidation states, coordination environments, and particle sizes on primary H_2O_2 selectivities, assessed by calculating the ratio of rate constants for the formation of H_2O_2 (via OOH* reduction; $k_{O\text{-}H}$) and the decomposition of OOH* (via O-O cleavage; $k_{O\text{-}O}$). For Pd metals, the $k_{O\text{-}H}/k_{O\text{-}O}$ ratio decreased from 10^{-4} for Pd(111) to 10^{-10} for Pd_{13} cluster at 300 K, indicating poorer H_2O_2 selectivity as Pd particle size decreases and low primary selectivities for H_2O_2 overall. As the oxygen chemical potential increases and metals form surface and bulk oxides, the perturbation of Pd-Pd ensemble sites by lattice O atoms results in selectivities that become dramatically higher than unity. For instance, at 300 K, the $k_{O\text{-}H}/k_{OO}$ ratio increases significantly from 10^{-4} to 10^{9} to 10^{16} as Pd(111) oxidizes to Pd_5O_4/Pd(111) and to PdO(100), respectively. In contrast, such selectivity enhancements are not observed for surface and bulk oxides that persistently contain rows of more metallic, undercoordinated Pd-Pd ensemble sites, such as PdO(101)/Pd(100) and PdO(101). These Pd-Pd ensembles are also absent when smaller Pd nanoparticles fully oxidize, indicating that smaller PdO clusters can be more selective for H_2O_2 synthesis. These trends for primary H_2O_2 selectivities were found to inversely correlate with trends for H_2O_2 decomposition rates via O-O bond cleavage, demonstrating that catalysts with high primary H_2O_2 selectivity can also hinder H_2O_2 decomposition. Ab-initio thermodynamics is used to estimate the thermodynamically favored phase among Pd, PdO/Pd and PdO in O_2, H_2O_2/H_2O, and O_2/H_2 environments. These results are combined to show that smaller Pd nanoparticles are more prone to be oxidized at lower oxygen chemical potentials, upon which they become more selective than larger Pd particles for H_2O_2 synthesis.

1. Introduction

Hydrogen peroxide (H_2O_2) is widely used in many industries, including textile processing, paper manufacturing, and wastewater treatments.[1,2] It is a "green" oxidant as it forms only H_2O as a by-product, making it an appealing choice for numerous industrial oxidation processes. However, the current industrial anthraquinone process for H_2O_2 production is cost-inefficient, environmentally unfriendly, and economically viable only at a large scale.[3,4] More recently, the direct synthesis of H_2O_2 from H_2 and O_2 ($H_2 + O_2 \rightarrow H_2O_2$; $\Delta H_{rxn}^0 = -188$ kJ mol^{-1})[5] has emerged as an alternative method to produce H_2O_2 at a smaller scale. The lower operating costs allow for geographically distributed H_2O_2 manufacturing, which could potentially mitigate safety risks in transporting concentrated H_2O_2.[3,4] Such a process can also be directly coupled with oxidative alkane conversions (i.e., methane oxidation to methanol) by forming H_2O_2 in-situ from H_2 and O_2 without extensive use of organic molecules.[6–10]

Palladium (Pd) is one of the most active metals for direct H_2O_2 synthesis but its commercial utilization is currently limited due to low H_2O_2 yields.[2,11–13] The major side reactions limiting H_2O_2 yields include H_2O formation either from reactants ($H_2 + O_2 \rightarrow H_2O + ½O_2$; $\Delta H_{rxn}^0 = -286$ kJ mol^{-1})[5] or from H_2O_2 decomposition ($H_2O_2 \rightarrow H_2O + ½O_2$; $\Delta H_{rxn}^0 = -98$ kJ mol^{-1}).[5] The primary H_2O_2 selectivity depends on the ability of catalysts to selectively reduce OOH* to H_2O_2* (where * represents adsorbed species), without cleaving the O-O bond in OOH* (step 4 vs. step 6 in Scheme 1).[2,12,14,15] The cleavage of the O-O bond in OOH* leads to the formation of O* and OH*, which ultimately leads to the formation of O_2 and H_2O via steps 7-11 in Scheme 1.[2,12] The H_2O_2 product formed can also decompose by cleaving its O-O bond (step 12; Scheme 1) and forming two hydroxyls (OH*) and ultimately O_2 and H_2O products (via step 11; Scheme 1). The low H_2O_2 selectivity and yield during the direct synthesis process on metallic Pd catalysts have been mainly attributed to the presence of Pd-Pd ensemble sites that tend to cleave O-O bonds in OOH* intermediates and H_2O_2 products.[16–19] Correspondingly, previous density functional theory (DFT) calculations showed that the O-O cleavage in bound OOH* and H_2O_2* (steps 6 and 12; Scheme 1) is very exothermic on metallic Pd surfaces. The reported reaction energies of steps 6 and 12 are -144 and -148 kJ mol^{-1} on Pd(111) and -176 and -220 kJ mol^{-1} and Pd(100), respectively, with very small activation barriers (< 20 kJ mol^{-1}) in all cases.[12]

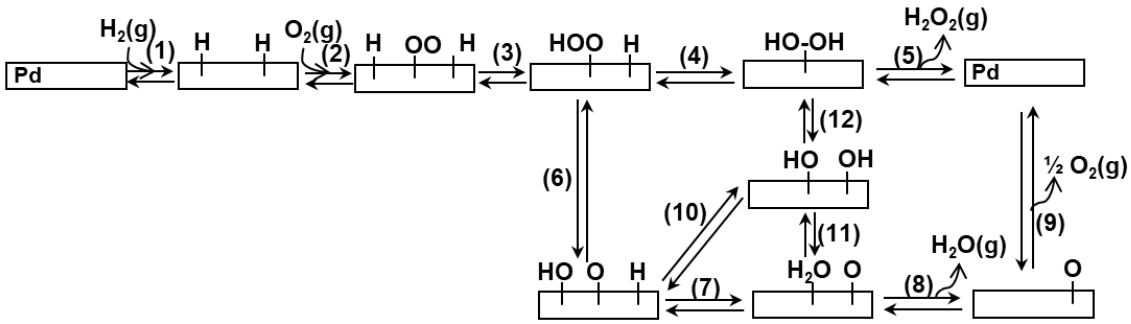

Scheme 1. Proposed elementary steps involved in direct H_2O_2 synthesis from H_2 and O_2 and H_2O_2 decomposition to form H_2O and ½ O_2.[12,14,20]

Previous literature has suggested that the oxidation states of Pd catalysts can significantly affect their H_2O_2 selectivities and yields.[15,21] This fact creates a critical knowledge gap in the mechanistic understanding of Pd-catalyzed direct H_2O_2 synthesis, given that the active phase of Pd nanoparticles during H_2O_2 synthesis and decomposition have remained controversial.[2,22,23] For instance, Kanungo *et al.* only detected metallic Pd during *in-situ* X-Ray absorption spectroscopy (XAS) measured at a range of H_2 and O_2 pressures (0-2 bar H_2, 0-2 bar O_2; 298 K; 20 vol% CH_3OH in H_2O with 0.05 M H_2SO_4).[22] In contrast, *in-situ* XAS studies by Adams *et al.* detected β-PdH_x upon exposure of Pd nanoparticles to H_2-rich condition (7 bar H_2, 0.6 bar O_2, 298K; in H_2O), which turned to surface oxides when subsequently exposed to O_2-rich condition (0.6 bar H_2, 10 bar O_2, 298K; in H_2O).[23]

Furthermore, the relative activities and selectivities of Pd, PdO, and PdH have been also debated in literature.[14,15,20,21,24] Wang *et al.* suggested PdO to be more active and selective for H_2O_2 synthesis than metallic Pd, with the support of DFT-derived O-O cleavage activation barriers for OOH* that were larger on PdO(101) than on Pd(111) (128 vs. 3 kJ mol^{-1} for step 6 in Scheme 1); the barriers for reducing OOH* (to form H_2O_2*) were slightly smaller for PdO(101) than for Pd(111) (44 vs. 56 kJ mol^{-1} for step 6 in Scheme 1).[15] Consistently, the pre-reduction of PdO/CeO_2 resulted in the significant decrease in H_2O_2 selectivity (from 56 % to 0 %; 0.017 bar H_2, 0.017 bar O_2; 295 K; in H_2O with 0.02 M H_2SO_4), which were attributed to increased H_2O_2 decomposition activities on metallic Pd nanoparticles.[24] Contradictory to these results, Adams *et al.* showed that pre-oxidized PdO/SiO_2 catalysts were inactive for H_2O_2 synthesis (0.05 bar H_2, 0.05 bar O_2; 298 K; in CH_3OH), and only became active once they were reduced under operating conditions (as evidenced by operando XAS).[23] We suggest that these controversies arise at least in part because the relevant phase of Pd and its corresponding activity/selectivity depend on the operating conditions (e.g., the reductant-to-oxidant (H_2/O_2) ratios, the operating temperature, and the solvent type)[2] and the size of the Pd nanoparticles.[25–27]

The effects of Pd particle sizes on H_2O_2 synthesis rates and selectivities have remained controversial. From kinetic measurements, Wilson *et al.* showed that H_2O formation during H_2O_2 synthesis

(via O-O cleavage in OOH* intermediates) is more facile on smaller Pd particles; measured activation enthalpy decreased from 32 to 18 kJ mol^{-1} as the average Pd diameter decreased from 7 to 0.7 nm, which they attributed to the difference in the electronic structure of these nanoparticles.[14] Measured enthalpic barriers for H_2O_2 formation, however, were similar for these particles (9-14 kJ mol^{-1}), from which they concluded that H_2O_2 synthesis selectivity can be enhanced by utilizing larger Pd particles. Such a conclusion is contradicted by Tian et al. who suggested that smaller Pd nanoparticles are more active and selective for H_2O_2 synthesis with minimal H_2O formation.[25] They found that H_2O_2 production rates (per surface Pd) increased from 191 to 284 (h^{-1}) and H_2O_2 selectivity increased from 43 to 94 %, as the average Pd particle sizes (from transmission electron microscopy) decreased from 2.6 to 1.6 nm. The authors suggested that these significant differences in selectivities originate from the existence of more Pd/PdO interfacial sites on sub-nanometer Pd particles, based on their ex-situ XAS and O_2 temperature-programmed desorption (TPD) measurements. These controversies support that particle size effects are also related to the reaction conditions and the oxidation states of Pd nanoparticles.

Herein we aim to deconvolute the effects of Pd particle sizes and their oxidation states on H_2O_2 synthesis and decomposition pathways by assessing DFT-derived energies of intermediates and transition states (TSs) on slab and particle models for metallic and partially oxidized Pd, as well as bulk PdO. In doing so, we demonstrate how Pd oxidation states and their surface structures influence primary H_2O_2 selectivity, which is dictated by kinetic preferences for either reducing OOH* or decomposing it to O* and OH* (steps 4 vs. 6; Scheme 1). The O-O cleavage in OOH* (step 6; Scheme 1) is very exothermic on all metallic Pd surfaces. Accordingly, the O-O cleavage activation barriers remain small both in absolute terms (< 30 kJ mol^{-1}) and relative to those for reducing OOH* to H_2O_2* (48-92 kJ mol^{-1}). This indicates a higher kinetic preference to decompose OOH* to O* and OH* on all Pd models, regardless of exposed facets (Pd(100), Pd(111)), particle sizes (Pd_{13} and Pd_{55}), and the coordination number (CN) of surface Pd atoms.

Our DFT calculations further support that kinetic preference can change to favor OOH* reduction (and H_2O_2 synthesis) once Pd form surface and bulk oxides. For example, the surface-oxidized Pd(111) surface (denoted as Pd_5O_4/Pd(111)) involves a higher barrier to cleave the O-O bond in OOH* than reducing OOH* to H_2O_2* (79 vs. 14 kJ mol^{-1}). However, whether such an enhancement occurs seems to depend not only on the oxidation state of Pd but also on the charge distribution and local geometric arrangement of surface Pd and O atoms. For instance, facet-dependent catalytic performance is found in PdO(100) and PdO(101), where the former is more selective towards H_2O_2 formation than the latter, even though Pd is formally found in a 2+ oxidation state on both surfaces. Given the apparent DFT-supported dependence of catalytic activity on the availability of Pd/PdO phases during direct H_2O_2 synthesis, we close our work with a discussion leveraging theory-derived phase diagrams for Pd in O_2, H_2O_2/H_2O and

O_2/H_2 environments to show how the size of Pd nanoparticles can impact their phase transformations and the resulting consequences on H_2O_2 synthesis and decomposition pathways.

2. Methods

2.1. Density functional theory (DFT) methods

Periodic DFT calculations were performed using the Vienna ab initio simulation package (VASP).[28] Planewaves were constructed using the projector-augmented wave (PAW) potentials[29] with an energy cutoff of 400 eV. The electron exchange correlations were described using the Purdue-Burke-Ernzerhof (PBE) functional.[30,31] Dispersion interactions were included using Grimme's D2 parameters.[32] Spin polarization was tested and applied for all calculations involving O-containing species. Ionic relaxations were performed using a conjugate gradient algorithm until the net force on each atom was less than 0.05 eV $Å^{-1}$. A convergence criterion of 10^{-6} eV was used for electronic energy minimizations, except during the calculation of vibrational modes, in which a stricter convergence of 10^{-7} eV was used. The Brillouin zone was sampled with Monkhorst-Pack[33] k-point grids of 9 x 9 x 9 for all bulk structures and 4 x 4 x 1 for all slab models, except for the Pd_5O_4/Pd(111) slab model (described below), which used Γ-point[34] sampling due to the large supercell size. All Pd, PdO/Pd, and PdO cluster models also used Γ-point sampling justified by the isolated nature of the cluster models. Additionally, the Hubbard U parameter is typically incorporated to account for strongly correlated d and f electrons in transition metal oxides. However, recent studies have suggested that while GGA+U simulations (U = 7 eV) improve band gap accuracy for PdO, they do not significantly impact the adsorption energies of intermediates.[35,36] Thus, standard DFT methods were used for all Pd, PdO/Pd, and PdO models.

DFT-derived lattice parameters of bulk Pd (3.907 Å) and PdO (a, b = 3.193 Å, c = 5.590 Å) were within 5% of the experimental values of Pd (3.889 Å)[37] and PdO (a, b = 3.043 Å, c = 5.336 Å).[38] These DFT-derived lattice parameters were used to construct slab models of Pd(111) and Pd(100), and PdO(100), and PdO(101) (Fig. 1), which represent the most stable and abundant facets in large Pd and PdO nanoparticles (> 5 nm).[12,39] The (4 x 4) supercells of Pd(111) and (100) slabs were modeled with four layers with 16 Pd atoms per layer, where the bottom two layers were kept fixed during simulations to mimic the bulk structure. The (2 x 3) supercells of PdO(100) and (101) slabs were constructed with two and four layers, respectively, where the bottom one and two layers remain fixed; each layer consists of 18 Pd-O pairs for PdO(100) and 12 Pd-O pairs for PdO(101). Previously reported models were leveraged here to describe the formation of thin oxide layers on Pd(111) and Pd(100) surfaces (Fig. 1).[40,41] Specifically, for Pd(111), a single layer of (√6x√6) Pd_5O_4 was placed on three layers of (4 x 12) Pd(111) (with the bottom layer fixed), inspired by scanning tunneling microscope (STM) images collected in ultra-high vacuum environments (10^{-7} to 10^{-5} mbar O_2; 570–683 K).[40,42,43] For Pd(100), a (√5x√5)R27° PdO(101) layer was placed on four

layers of (4x4) Pd(100) (with the bottom two layers fixed),[44] inspired by observations of a (√5x√5)R27° PdO(101) structure in STM images upon exposure of Pd(100) to O_2 pressures up to 1 bar at temperatures < 600 K.[41,45] All slab models included a vacuum layer (15 Å) in the z-direction to prevent any artifacts caused by periodic boundary conditions.

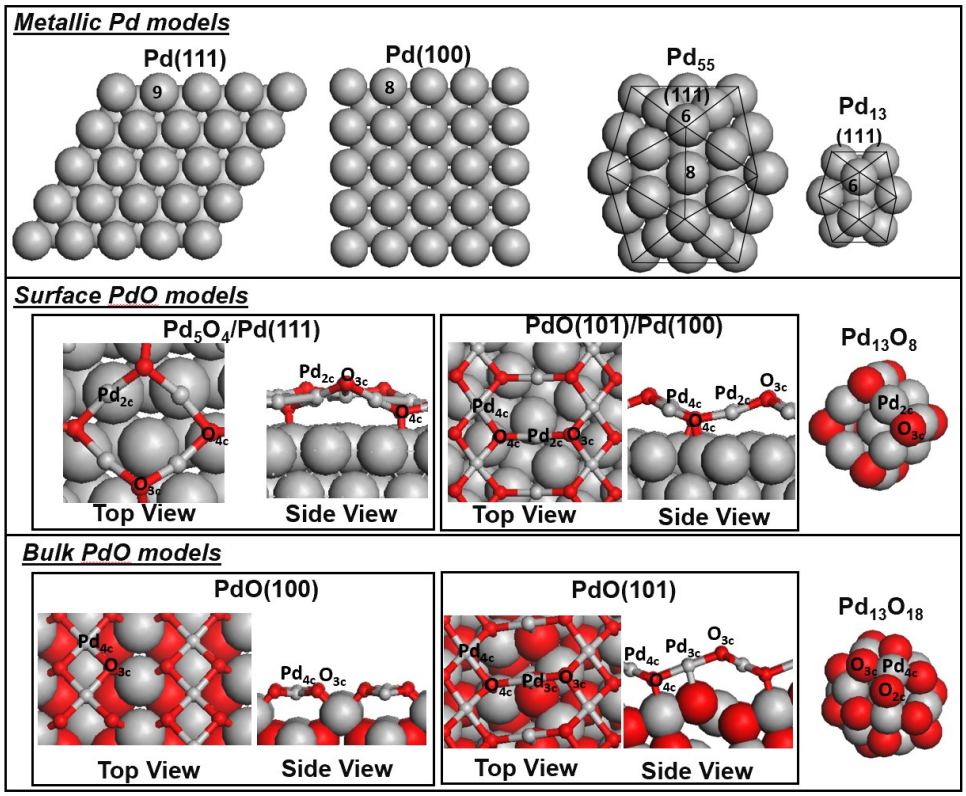

Figure 1. DFT-derived structural models for metallic Pd, surface oxides, and bulk PdO; these structures are also provided in the Supporting Information. Light grey represents Pd and red represents O. The coordination number (CN) of surface Pd and O atoms are shown as numbers (in metallic Pd models) and as subscripts (in surface oxide and bulk oxide models) where the CN for Pd refers to the number of O atoms it is coordinated to, and the CN for O refers to the number of Pd atoms it is coordinated to.

Pd_{13} and Pd_{55} clusters were used to model Pd nanoparticles of ~0.5 and 0.9 nm in diameter. The distorted Pd_{13} icosahedron[46–49] exclusively contains (111) facets, where one central atom is surrounded by 12 surface Pd atoms (CN = 6; Fig. 1). The "atom on hollow site" packing of additional layers to this 13-atom cluster leads to the Pd_{55} Mackay icosahedron, containing 42 Pd atoms at the outer shell (CN = 6 and 8 for corner and edge sites, respectively; Fig. 1).[50,51] These clusters were constructed by cleaving DFT-derived Pd bulk structure and placing them at the center of 20 x 20 x 20 and 30 x 30 x 30 $Å^3$ simulation boxes, respectively. All Pd atoms in the Pd clusters were fully relaxed, except the central Pd atom, which was kept fixed to prevent translational movement of the cluster during simulations. DFT-optimized structures were used as input configurations for classical molecular dynamics (MD) simulations (described

in Section 2.2) to identify other possible Pd_{13} and Pd_{55} clusters with lower energies. To minimize the error associated with MD simulations, all clusters suggested from MD simulations were iteratively re-optimized using DFT methods. Such a DFT/MD/DFT iteration process allowed us to identify Pd_{13} and Pd_{55} clusters with lower energies than those of the initially proposed structures, with the final structures being shown in Figure 1; the final geometries of these structures are also provided in the Supporting Information.

Analogous DFT/MD/DFT iterations were used to search for low-energy cluster models for PdO. In one approach (method I), we sequentially added O atoms on the optimized Pd_{13} cluster and optimized each structure with DFT at each additional step until the target number of O-atoms was reached. These DFT-derived structures were then taken as inputs for classical MD simulations that were used to suggest other low-energy structure candidates for subsequent testing via DFT. In another approach (method II), the input structures for classical MD simulations were derived from $Pd_{13}O_x$ clusters (x = 6-15) cleaved from bulk PdO. The structures identified from method I resulted in lower energies than those from the second approach. The comparison between the two models is detailed in Section S1 in Supporting Information (SI). The final clusters with the lowest energies (in Fig. 1) were further used to probe the energies of intermediates and TSs in H_2O_2 synthesis and decomposition pathways via DFT.

At least 1 to 10 initial binding configurations of intermediates and product states were probed on all possible binding sites within each surface to locate the structures with lowest energies. The comparisons among binding sites are discussed in Section S3, but only the configurations with the most favorable binding energies are discussed here. Initial and product states of each elementary step were connected with 4 to 8 images using the nudged elastic band (NEB) method.[52,53] The highest-energy image along the reaction coordinate was used as the initial guess for the TS search using the dimer method.[54] All NEB calculations used a convergence threshold of 10^{-4} eV for electronic energies and 0.05 eV $Å^{-1}$ for forces on each atom. The dimer methods used tighter convergence thresholds of 10^{-6} eV for electronic energies and 0.05 eV $Å^{-1}$ for forces. The oxidation states of each atom were obtained from Bader charge analysis.[55]

DFT-derived vibrational modes of adsorbed species and gas-phase molecules were determined using a finite difference method,[56] where elements of the Hessian matrix were obtained by systematically perturbing atom positions by 0.015 Å in ± x, ± y, and ± z directions. During these calculations, all adsorbates were fully relaxed while the surface structures were kept fixed. Obtained vibrational frequencies were used to calculate partition functions within the harmonic oscillator approximation to derive zero-point vibrational energies (ZPVE) and enthalpies (H), and entropies (S) at finite temperatures and relevant pressure (1 bar) using statistical mechanical formalisms, which in turn were used to calculate free energies.[57] The low modes (< 100 cm^{-1}) of weakly bound intermediates represent frustrated translational and rotational modes of molecules upon adsorption on the surface, which may not be accurately captured within the harmonic oscillator approximation.[58] These modes may impose errors in calculating entropies and thus are removed

in calculating entropies and free energies. Alternatively, these low modes can be replaced by a 70% contribution of the average of translational and rotational entropy of the molecule in the gas phase, inspired by experimental observations by Campbell *et al*.[59] The free energy diagrams calculated with this method were compared with those calculated with the first approach in Fig. S23 (in SI), which give the upper and lower bounds of free energies.

2.2. Moecular dynamic (MD) simulations

Classical MD simulations in the NVT ensemble (with a 0.25 fs timestep) were performed using the LAMMPS software (29/Sep/2021 stable version).[60] The reactive force-field ReaxFF[61–63] was used with the parameters designed to capture interatomic interactions in Pd-O systems.[63] To validate the practicality of the force field for Pd and PdO systems, lattice parameters were calculated for bulk Pd and PdO though expansion-compression calculations (Figs. S2 and S3). The lattice constant of bulk Pd determined from ReaxFF MD simulations (3.97 Å) agreed well with values from DFT-estimation (3.907 Å) and experiments (3.889 Å)[37], with errors less than 1%. The lattice constants for PdO from ReaxFF MD were a=b=2.907 and c=5.253 Å, which were also in good agreement with the DFT estimated constants (a=b=3.193 Å and c=5.590 Å) and experimental values (a=b=3.043 Å and c=5.336 Å)[38], with errors less than 5%.

For each MD simulation, the Pd or Pd_xO_y cluster was located at the center of the 30 x 30 x 30 $Å^3$ simulation box. Initial atom positions were relaxed using a conjugate gradient algorithm[64] until the cluster energy changed less than 0.0001 % with respect to the preceding geometry. For method I (see Section 2.1), the Nose-Hoover thermostat[65] was used with a 25 fs damping through stages of heating and cooling. Following a 0.125 ns equilibration stage at 200 K, temperature was ramped up to 400 K within a 0.250 ns timeframe and maintained at that temperature for additional 0.125 ns. Then, the temperature was ramped up from 400 to 1200 K within a 0.125 ns timeframe and maintained at that temperature for 0.250 ns to provide the system with enough energy to potentially hop between different minima within the timeframe of the simulation. Successively, the temperature was ramped down from 1200 to 400 K and from 400 to 200 K using the same time frames used for the heating stages. For method II (see Section 2.1), the Berendsen thermostat[66] was used with a 25 fs damping parameter, and configurations of the Pd_xO_y cluster were sampled over a single 0.750 ns stage of equilibration at 700 K. The initial screening of clusters obtained from method II resulted in configurations that were much more unstable than those obtained from method I. For this reason, the method II clusters were only sampled through constant temperature MD runs rather than the more computationally intensive heating/cooling MD runs. In all cases, the Pd and Pd_xO_y clusters with the lowest potential energies were identified and reoptimized using DFT methods (as detailed in Section S1; SI).

2.3. Ab-initio thermodynamic calculations

Phase diagrams of Pd-PdO transformations were assessed by calculating the most thermodynamically favored states of Pd-O systems in O_2, H_2O_2/H_2O or O_2/H_2 environments. For a system in a grand canonical ensemble, the number of atoms fluctuates to minimize the grand potential (Φ) at a given set of conditions. For Pd in an oxidizing environment, the grand potential of the system ($\Phi_{N_{Pd}N_O}$) depends on temperature and the chemical potentials of Pd* and O* ($\mu_{Pd*}$and μ_{O*}):[67]

$$\Phi_{N_{Pd}N_O}(T, \mu_{Pd*}, \mu_{O*}) = F_{N_{Pd}N_O}(T) - N_{Pd}\mu_{Pd*} - N_O\mu_{O*} \quad (1)$$

where N_{Pd} and N_O are numbers of Pd and O atoms in the solid phase, respectively. $F_{N_{Pd}N_O}$ represents the Helmholtz free energy, which includes the internal energy (approximated as its DFT-calculated electronic energy, $E^{DFT}_{N_{Pd}N_O}$), the vibrational contributions to the Helmholtz free energy ($F^{vib}_{N_{Pd}N_O}(T)$), and the configurational entropy contribution to the Helmholtz free energy at a given temperature T (TS^{conf}):

$$F_{N_{Pd}N_O}(T) = E^{DFT}_{N_{Pd}N_O} + F^{vib}_{N_{Pd}N_O}(T) - TS^{conf} \quad (2)$$

As contributions from vibrations (<0.01 eV/Å^2) and configurational entropies (< ~0.003 eV/Å^2, based on Reuter and Scheffler's method[68]) are negligible in the 300-1000 K temperature range, the electronic energy was assumed to be the main contributor to the total Helmholtz free energy; these contributions are shown in Figure S9 (SI) as a function of temperature. Accordingly, the grand potential can be simplified as:

$$\Phi_{N_{Pd}N_O} = E^{DFT}_{N_{Pd}N_O} - N_{Pd}\mu_{Pd*} - N_O\mu_{O*} \quad (3)$$

Upon oxidation of the clean Pd surface, the change in the grand potential ($\Delta\Phi$) is given by:

$$\Delta\Phi = E^{DFT}_{N_{Pd}N_O} - E^{DFT}_{N_{Pd}} - \left(N_{Pd,PdO} - N_{Pd,clean}\right)\mu_{Pd*} - N_O\mu_{O*} \quad (4)$$

where $E^{DFT}_{N_{Pd}}$ and $E^{DFT}_{N_{Pd}N_O}$ are DFT-derived electronic energies of discrete Pd surfaces before and after oxidation, and $N_{Pd,clean}$ and $N_{Pd,PdO}$ are the number Pd atoms in the metallic and oxidized states. The chemical potential of O* (μ_{O*}) is determined by the chemical potential of gas-phase oxidants. For instance, as Pd-PdO oxidation driven by O_2 can be written as:

$$Pd_x + \frac{y}{2}O_2 \rightarrow Pd_xO_y \quad , \quad (5)$$

in such case, μ_{O*} is set by the chemical potential of O_2.

$$\mu_{O*} = \frac{1}{2}\mu_{O_2} \quad (6)$$

On the other hand, when Pd-PdO oxidation is driven by H_2O_2:

$$Pd_x + yH_2O_2 \rightarrow Pd_xO_y + yH_2O \quad , \quad (7)$$

$\mu_{O*}$is set by the difference in the chemical potentials of H_2O_2 and H_2O.

$$\mu_{O*} = \mu_{H_2O_2} - \mu_{H_2O} \quad (8)$$

The chemical potential of a gas-phase species i, μ_i, can be calculated as:

$$\mu_i = \mu_i^o + k_B T ln\left(\frac{f_i}{f^0}\right) \tag{9}$$

where f^0 is the reference fugacity (chosen to be 1 bar), f_i is the fugacity of gas-phase species i. μ_i^o is the reference chemical potential:

$$\mu_i^o(T) = H_i{}^o(T) + E_i^{DFT} + E_i^{ZPVE} - H_i{}^o(0\ K) - T\ S_i{}^o(T) \quad , \tag{10}$$

where $H_i{}^o$ is the standard molar enthalpy, E_i^{DFT} is the DFT-calculated electronic energy, E_i^{ZPVE} is the zero-point energy, and $S_i{}^o$ is the standard molar entropy. The μ_i^o values for O_2, H_2O_2, H_2O, and H_2 are calculated using the standard enthalpy and entropy values listed in the JANAF thermochemical tables (p^0=1 bar; 100-1000 K)[69] and are listed in Table S1. The JANAF values agree well (within a 0.2% error) with reference chemical potentials calculated from first principles[57] as shown in Section S2 (SI).

At low to moderate pressures, the fugacity of gas-phase species i is approximated by its partial pressure p_i. Hence the chemical potential μ_{O*} can be calculated as:

$$\mu_{O*}(T,P) = \frac{1}{2}\left(\mu_{O_2}^o(T) + k_B T ln\left(\frac{p_{O_2}}{p^0}\right)\right) \tag{11}$$

$$\mu_{O*}(T,P) = \mu_{H_2O_2}^o(T) - \mu_{H_2O}^o(T) + k_B T ln\left(\frac{p_{H_2O_2}}{p_{H_2O}}\right) \tag{12}$$

where Eq. 11 and Eq. 12 respectively apply to cases where O_2 and H_2O_2 are the oxidants. As done in previous studies,[40,44,45] the reference state for calculating μ_{O*} was chosen to be gas-phase O_2. Phase diagrams were then built by calculating the change in the grand potential ($\Delta\Phi$) over a range of μ_{O*} for different Pd-O systems (via Eq. 4) and identifying the configurations that minimize $\Delta\Phi$.

In the phase diagrams, it is reasonable to assume that there are upper and lower limits of μ_{O*} at which PdO is stable. The lower limit of μ_{O*} is set under oxidant-poor conditions at which the bulk oxide decomposes into gas-phase oxidant and metallic Pd:

$$\mu_{PdO*}^{bulk} < \mu_{Pd*}^{bulk} + \mu_{O*} \tag{13}$$

At T = 0 K, the Gibbs free energy of formation for PdO ($\Delta G_{f,PdO}$) is given by $\mu_{PdO}^{bulk} - \mu_{Pd*}^{bulk} - \frac{1}{2}\mu_{O_2}$, which can be approximated with DFT-derived electronic energies:

$$\Delta G_{f,PdO} = E_{PdO}^{DFT} - E_{Pd}^{DFT} - \frac{1}{2}(E_{O_2}^{DFT} + E_{O_2}^{ZPVE}) = -0.87\ eV \tag{14}$$

The DFT-derived $\Delta G_{f,PdO}$ value (-0.87 eV) agrees well with the experimental value (-0.97 eV[70]) and thus was used as a boundary condition. The upper limit of μ_{O*} is set under oxidant-rich conditions, at which the formation of gas-phase oxidant is preferred over O* adsorption:

$$0 > \mu_{O*} \tag{15}$$

Thus, the phase diagrams further discussed in Section 3.4 utilize -0.87 eV < μ_{O*}< 0 eV as the bounds for PdO formation on metallic Pd surfaces. To construct T, p phase diagrams for each phase, the range of temperatures and pressures for each oxidant is calculated from the μ_{O*} (via Eqns. 11 and 12) at which each phase becomes stable. In these diagrams, the range of temperatures (200 to 1000 K) and gas-phase O_2 pressures (10^{-15} bar to 100 bar) are chosen to be representative of experimental UHV conditions from previous metal oxidation studies[40,42,43,45] and relevant H_2O_2 synthesis conditions.[2,14,20] The calculation details for deriving the phase diagrams in O_2 and H_2 mixtures, following the procedure reported by Chen *et al.*[20], are described in Section S2 in SI.

3. Results and Discussion

3.1 DFT assessments of H_2O_2 synthesis pathways on Pd, PdO/Pd and PdO catalysts

We start our discussion with the energetics of H_2O_2 synthesis and decomposition on metallic Pd. The plausible H_2O_2 synthesis and decomposition pathways that agree with previous theoretical works are shown in Scheme 1.[2,2016] The proposed reaction pathways are also consistent with the negligible formation of $H^{18}O^{16}OH$ when reacting H_2 with $^{16}O_2$ and $^{18}O_2$ mixtures, implying reactions of H* with intact O_2* in forming H_2O_2.[71] More recent studies by Ricciardulli et al.[16] suggested the possible involvement of protonic solvents (e.g., H_2O) that lower the O_2* reduction activation barriers by mediating proton coupled electron transfer.[16] Although relevant, the assessment of solvent-mediated pathways is beyond the scope of this work, which focuses on the effects of Pd oxidation states and particle sizes on the primary H_2O_2 selectivities and yields.

Figure 2 shows DFT-derived free energies of intermediates and TSs involved in the plausible elementary steps (Scheme 1) for H_2O_2 synthesis (solid pathway) and decomposition (dashed pathways) on the clean Pd(111) surface. Free energies were calculated at 300 K and 1 bar as relevant to the H_2O_2 synthesis process.[22,8,14,21,25] For reference, DFT-derived electronic energies (without any corrections) and relevant structures for Pd(111) are shown in Figure S25 (SI).

Dissociative H_2 adsorption on Pd(111) forms two H* via an exoergic step (ΔG_{300K} = -114 kJ mol^{-1}; Fig. 2; step 1 in Scheme 1); such a step is expected to be nearly barrierless, as suggested from previous DFT calculations.[72] Molecular O_2 adsorption occurs in a step that is only slightly exoergic (ΔG_{300K} = -28 kJ mol^{-1}; step 2 in Scheme 1). Previous studies have suggested the formation of physisorbed O_2 (d_{O-O} = 0.124 nm), superoxo (O_2^-, d_{O-O} = 0.134 nm) or peroxo (O_2^{2-} d_{O-O} = 0.137 nm) complexes on Pd(111) surfaces.[73,74] O_2* exhibits an O-O bond length of 0.137 nm and gains charge from Pd based on Bader charge analysis[55] (-0.54e; Fig. S34), suggesting that O_2* is more likely to be in an O_2^{2-} state on Pd(111). Similar trends were observed on all metallic Pd models, where bound O_2* species gained charged upon adsorption (-0.69e, -0.62e, and -0.63e on Pd(100), Pd_{55}, Pd_{13}, respectively) with elongated O-O bonds (0.143, 0.139, and 0.138

nm), indicative of the O_2^{2-} species (Fig. S34; SI). This activated O_2* reacts with H* to form OOH* (step 3; Scheme 1). This first H-transfer step has a reaction free energy of -7 kJ mol^{-1} and activation free energy barrier of 50 kJ mol^{-1}. The second H-transfer to OOH* forms H_2O_2* (step 4; Scheme 1), with a reaction free energy of -13 kJ mol^{-1} and a free energy barrier of 35 kJ mol^{-1}. Finally, H_2O_2* desorbs in an endoergic step (ΔG_{300K} = +41 kJ mol^{-1}; step 5 in Scheme 1), closing the catalytic cycle.

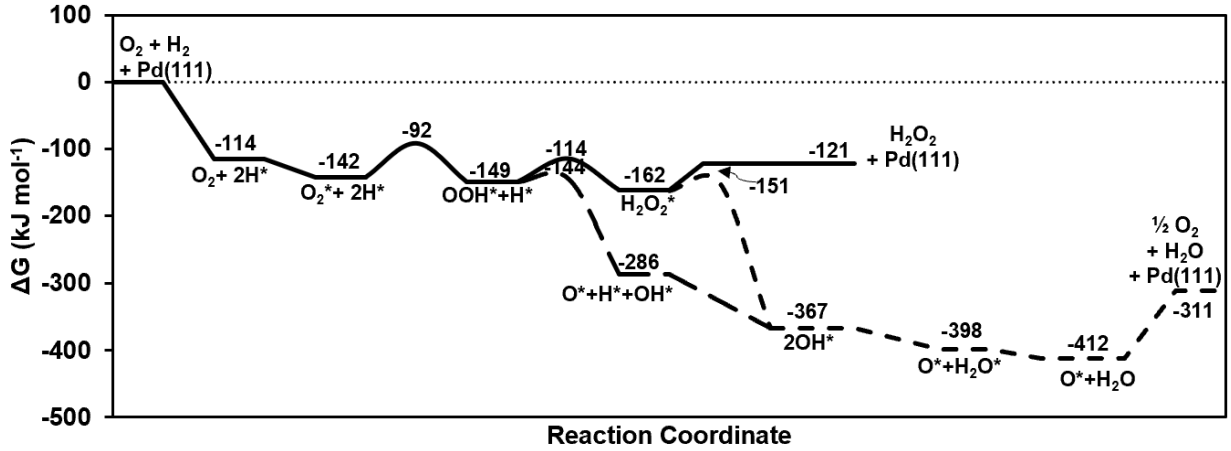

Figure 2. DFT-derived free energies (300 K; 1 bar) of intermediates and TSs involved in H_2O_2 synthesis and decomposition elementary steps (from Scheme 1) on Pd(111); the free energies of O_2 and H_2 and Pd(111) are used as reference. Corresponding structures and their electronic energies (without any corrections) are shown in Figure S25 (SI).

Alternatively, once the OOH* intermediate is formed, it can cleave its O-O bond to form O* and OH* in a very exoergic step (ΔG_{300K} = -137 kJ mol^{-1}; step 6 in Scheme 1) with a free energy barrier of 5 kJ mol^{-1}. The resulting OH* can react with H* to form H_2O* via another exoergic step (ΔG_{300K} = -112 kJ mol^{-1}; step 7 in Scheme 1). Although surface O* may desorb as O_2 via recombinative desorption (step 9 in Scheme 1), such a step is very endoergic (ΔG_{300K} = +101 kJ mol^{-1}), suggesting high surface coverages of O* during steady-state catalysis especially at high O_2/H_2 ratios. At high H* coverages (at low O_2/H_2), O* species may react with H* to form OH* (ΔG_{300K} = -81 kJ mol^{-1}; step 10 in Scheme 1), which ultimately forms H_2O via steps 7 and 8 (in Scheme 1).

The H_2O_2* formed can also decompose as it cleaves its O-O bond, forming two OH* (step 12; Scheme 1). This step is very exoergic (ΔG_{300K} = -205 kJ mol^{-1}) with a free energy barrier of +11 kJ mol^{-1}. OH* species can react via step 11 (in Scheme 1) to form H_2O* and O* (ΔG_{300K} = -31 kJ mol^{-1}). Energy diagrams revealing similar trends were obtained for clean Pd(100) surface, and clean Pd_{55} and Pd_{13} particles, as shown in Figures S26–S28 (in SI). Overall, the formations of O* and OH* from OOH* and H_2O_2* decomposition pathways are very exoergic on all clean Pd models, suggesting that all facets in both large and small Pd particles are readily populated with surface-bound O* and/or OH* species.

Next, we consider the energetics of H_2O_2 synthesis and decomposition on PdO/Pd systems. Upon exposure to oxidizing conditions, epitaxial surface oxide layers can form on metallic Pd, where the oxide structure is influenced by the structures of the metal layers below.[40,41] For instance, the oxide layer formed on Pd(111) contains reactive Pd atoms in 2-fold coordination and O atoms in 3-fold coordination (Pd_{2c} and O_{3c}), along with unreactive 4-coordinated O atoms (O_{4c}) (see Pd_5O_4/Pd(111) in Fig. 1). Figure 3 illustrates the free energies of relevant intermediates and TSs on Pd_5O_4/Pd(111).

Dissociative H_2 adsorption on a vicinal O_{3c} pair in Pd_5O_4/Pd(111) occurs in an exoergic step (ΔG_{300K} = -93 kJ mol^{-1}; Fig. 3). Molecular O_2 adsorption is only slightly exoergic, where O_2 binds at a bridge site between two Pd_{2c} atoms (ΔG_{300K} = -14 kJ mol^{-1}). This O_2* seems to represent O_2^- species, evidenced by its O-O distance (0.133 nm), which is within the literature range of superoxo species, ~0.13 nm,[74,75] and net charge gain (-0.37e; Fig. S34) that is less negative than O_2^{2-} species on metallic Pd models (-0.69e to -0.54e; Fig. S34). This activated O_2* reacts with H* to form OOH* atop of Pd_{2c} (ΔG_{300K} = -35 kJ mol^{-1}) in a nearly barrierless step. Subsequently, OOH* can react with H* to form H_2O_2* (ΔG_{300K} = -4 kJ mol^{-1}) in another nearly barrierless step. H_2O_2* formed can desorb in a following step, completing the synthesis pathway (ΔG_{300K} = +25 kJ mol^{-1}). Alternative to H_2O_2* formation, the O-O bond in OOH* could cleave on vicinal Pd_{2c} atoms in an exoergic reaction step (ΔG_{300K} = -69 kJ mol^{-1}), forming O* and OH*, both adsorbed at bridge sites between two Pd_{2c} atoms. However, this OOH* cleavage step faces a higher free energy barrier than the O-H formation step ($\Delta G^{\ddagger}_{300K}$ = 74 vs. ~0 kJ mol^{-1}; Fig. 3). In contrast, the O-O bond cleaves more easily in H_2O_2* to form two OH* groups in an exoergic step (ΔG_{300K} = -148 kJ mol^{-1}; $\Delta G^{\ddagger}_{300K}$ = 13 kJ mol^{-1}; Fig. 3). However, the subsequent disproportionation of two OH* to form O* and H_2O* is very endoergic (ΔG_{300K} = +73 kJ mol^{-1}), suggesting that this surface oxide may prefer to maintain a high surface coverage of OH*. Still, in comparison to Pd(111), the O-O cleavage barrier for OOH* is higher in Pd_5O_4/Pd(111) (74 vs. 5 kJ mol^{-1}), suggesting that OOH* decomposition is less preferred on this surface.

The other surface oxide models explored include $Pd_{13}O_8$ and PdO(101)/Pd(100) (Fig. 1). The $Pd_{13}O_8$ cluster behaves similarly to Pd_5O_4/Pd(111) in the facile formation of H_2O_2*, with higher activation barriers for O-O cleavage in OOH* than O-H bond formation ($\Delta G^{\ddagger}_{300K}$ = 66 vs. 48 kJ mol^{-1}; Fig. S31). In contrast, O-O cleavage in OOH* is slightly preferred over O-H formation on PdO(101)/Pd(100) ($\Delta G^{\ddagger}_{300K}$ = 109 vs. 112 kJ mol^{-1}; Fig. S30), highlighting the dependance of the favored reaction pathway on the type of surface oxide formed and the Pd structure underneath. The details of structural differences among these surface oxide models and their consequences on rates and selectivities are discussed in Section 3.2. Gibbs free energy and electronic energy diagrams for PdO(101)/Pd(100) and $Pd_{13}O_8$ are shown in Figures S30 and S31, respectively, along with the relevant structures for intermediates and TS structures.

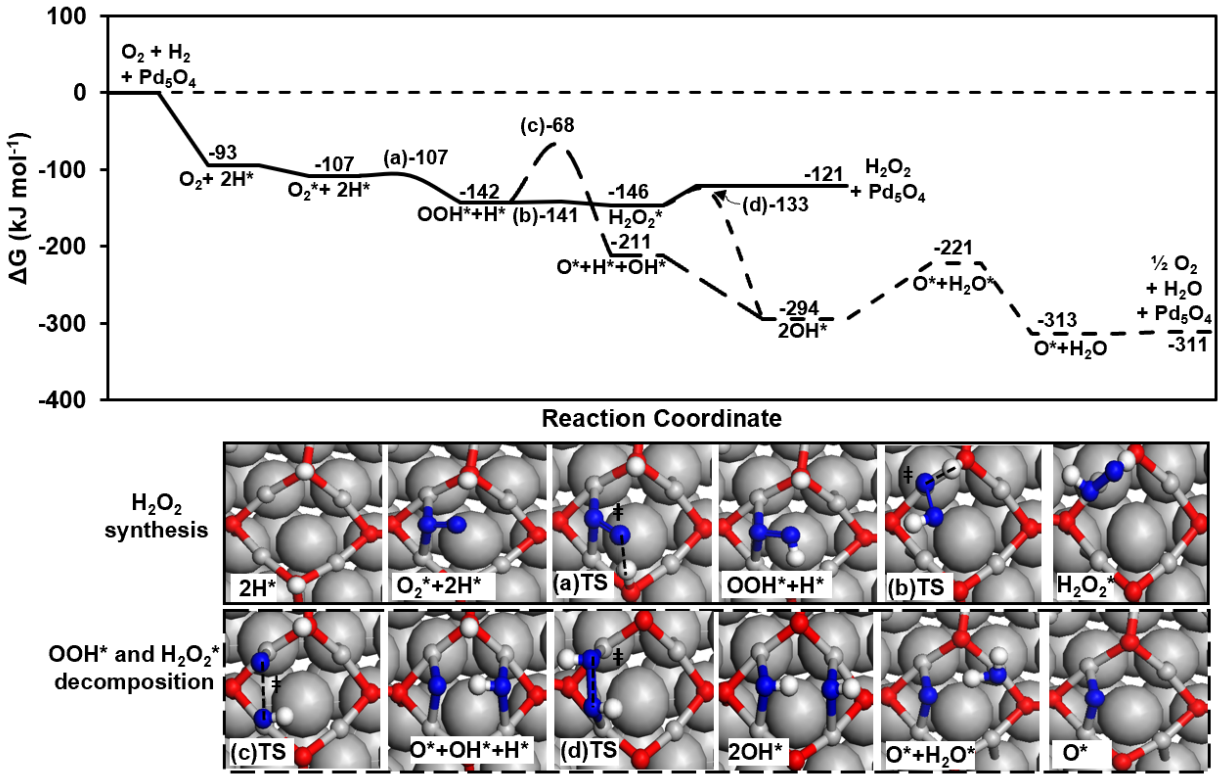

Figure 3. DFT-derived free energies (300 K; 1 bar) of intermediates and TSs involved in H_2O_2 synthesis and decomposition elementary steps (from Scheme 1) on Pd_5O_4/Pd(111); the free energies of O_2 and H_2 and Pd_5O_4/Pd(111) are used as reference. Electronic energies (without any corrections) are shown in Figure S29 as a reference.

Given suitable oxidizing conditions, the formation of surface oxides can be followed by a complete transformation of Pd into bulk PdO. Thus, we now discuss the energetics of H_2O_2 synthesis and decomposition on PdO(101) and PdO(100), the low index facets in bulk PdO. PdO(101) contains alternating rows of undercoordinated Pd_{3c} and fully-coordinated Pd_{4c} atoms, which are connected with undercoordinated O_{3c} and fully-coordinated O_{4c} atoms (Fig. 1). The O_{3c} atoms bind H* strongly with dissociative H_2 adsorption being exoergic (ΔG_{300K} = -129 kJ mol^{-1}; Fig. 4). The molecular O_2 adsorption free energy is also very exoergic, where O_2* interacts with two vicinal Pd_{3c} atoms (ΔG_{300K} = -129 kJ mol^{-1}). The O-O distance in O_2* (0.133 nm) is consistent with those in the superoxo species (~0.13 nm);[74,75] this O_2* moiety also gains charge upon adsorption (-0.42e; Fig. S34). This activated O_2* readily reacts with H* to form an OOH* that interacts with vicinal Pd_{3c} atoms in a bridge configuration in a nearly barrierless step (ΔG_{300K} = +5 kJ mol^{-1}; $\Delta G^{\ddagger}_{300K}$ ~ 0 kJ mol^{-1}). The OOH* species can further react with H* to form H_2O_2* with a moderate free energy barrier (ΔG_{300K} = +44 kJ mol^{-1}; $\Delta G^{\ddagger}_{300K}$ = 49 kJ mol^{-1}). However, it is more facile to cleave the O-O bond in OOH* to form O* and OH*, as this step is more exoergic and faces a lower free energy barrier (ΔG_{300K} = -87 kJ mol^{-1}, $\Delta G^{\ddagger}_{300K}$ = 11 kJ mol^{-1}). Even if H_2O_2* is formed on PdO(101),

its decomposition is thermodynamically and kinetically favorable. The O-O bond elongation and cleavage in H_2O_2* across two Pd_{3c} sites occurs in a very exoergic step (ΔG_{300K} = -219 kJ mol^{-1}) and is nearly barrierless ($\Delta G^{\ddagger}_{300K}$ = 3 kJ mol^{-1}). Although the OH* species resulting from the decomposition can further react in a disproportionation step to form H_2O* and O*, this step is quite endoergic (ΔG_{300K} = +90 kJ mol^{-1}) suggesting that OH* species may be the most abundant intermediate on this surface.

The low barriers and exothermic reaction energies for O-O cleavage in OOH* and H_2O_2* suggest low H_2O_2 selectivities and yields on PdO(101) during H_2O_2 synthesis, which we attribute to the presence of rows of adjacent, undercoordinated Pd_{3c} atoms that allows for facile O-O cleavage in a manner similar to metallic Pd surfaces. Notably, the results herein contradict previous DFT calculations by Wang *et al.*,[15] who concluded that PdO(101) is highly selective for H_2O_2* synthesis. On PdO(101), these authors found higher activation barriers for O-O cleavage in OOH* (128 kJ mol^{-1}) and H_2O_2* (74 kJ mol^{-1}) possibly due to not accounting for possible O-O bond elongation over Pd_{3c} sites (which results in a more stable TS and allows for facile O-O cleavage as we show here). A separate DFT study by Li *et al.* found that H_2O_2* readily dissociates into two OH* at Pd_{3c} atoms on PdO(101),[76] a result that agrees well with our calculations.

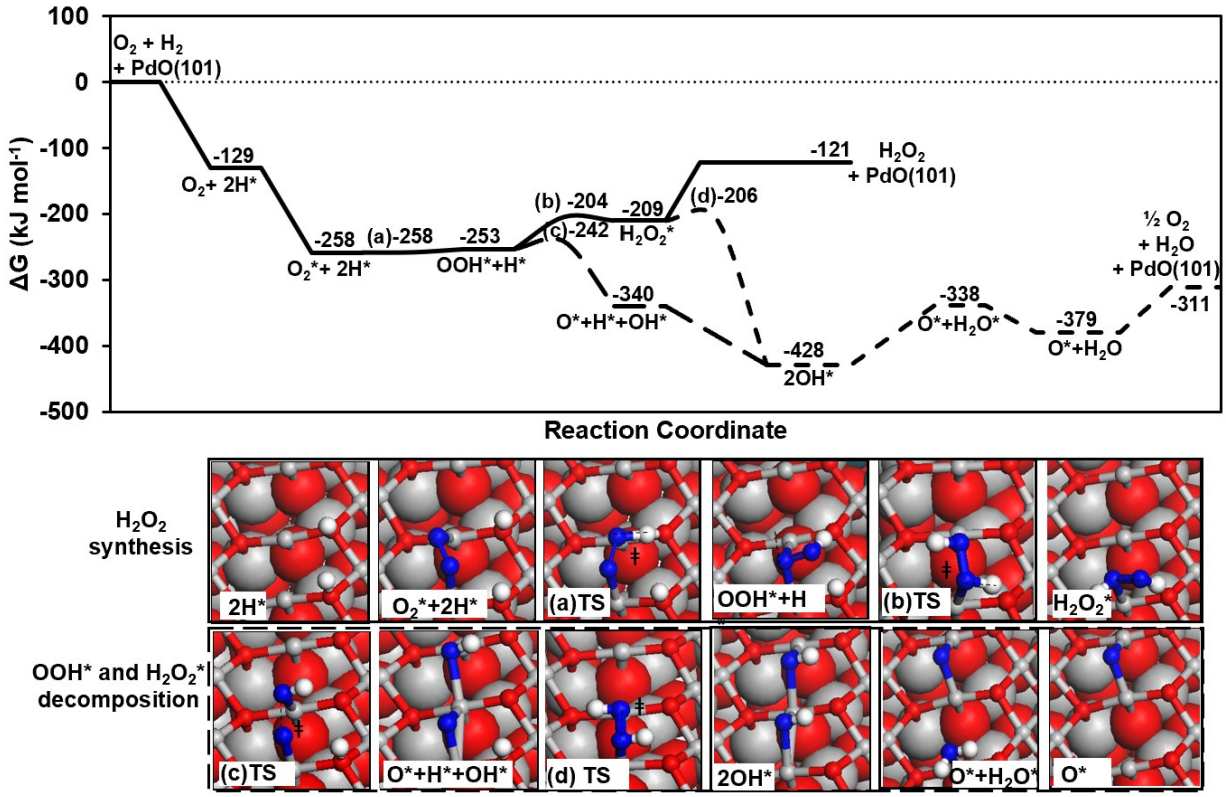

Figure 4. DFT-derived free energies (300 K; 1 bar) of intermediates and TSs involved in H_2O_2 synthesis elementary steps (from Scheme 1) on PdO(101); the free energies of O_2 and H_2 and PdO(101) are used as reference. Electronic energies (without any corrections) are shown in Figure S32 as a reference.

In contrast to PdO(101), PdO(100) does not present adjacent undercoordinated Pd_{3c} atoms; it consists of Pd atoms all in 4-fold coordination (Pd_{4c}) and of O-atoms all in 3-fold coordination (O_{3c}). Dissociative adsorption of H_2 on a vicinal O_{3c} pair in PdO(100) is very exergonic (ΔG_{300K} = -241 kJ mol^{-1}; Fig. 5), even more so than that on PdO(101) (-129 kJ mol^{-1}; Fig. 4), underlining the reactive nature of O_{3c} atoms in PdO(100). On the other hand, Pd_{4c} atoms in PdO(100) are less reactive than in PdO(101), as indicated by molecular O_2 adsorption atop a Pd_{4c} site being endoergic (ΔG_{300K} = +30 kJ mol^{-1}). The adsorbed O_2* has an O-O distance of 0.124 nm, consistent with that of O_2(g) (0.124 nm). Correspondingly, Bader charge analysis shows that this O_2* on PdO(101) gains negligible charge upon adsorption (-0.08e; Fig. S34). This physisorbed O_2* can react with H* to form OOH* with a moderate free energy barrier (ΔG_{300K} = +39 kJ mol^{-1}; $\Delta G^{\ddagger}_{300K}$ = 40 kJ mol^{-1}). Note that this OOH* is adsorbed atop a Pd_{4c} site, where its H* atom forms a H-bond with a surface O_{3c} atom. OOH* can then react with H* to form H_2O_2* in a slightly endoergic step (ΔG_{300K} = +38 kJ mol^{-1}; $\Delta G^{\ddagger}_{300K}$ = 39 kJ mol^{-1}). In contrast, the alternative step involving O-O bond cleavage in OOH* is more endoergic (+136 kJ mol^{-1}) and faces a higher free energy barrier (+164 kJ mol^{-1}).

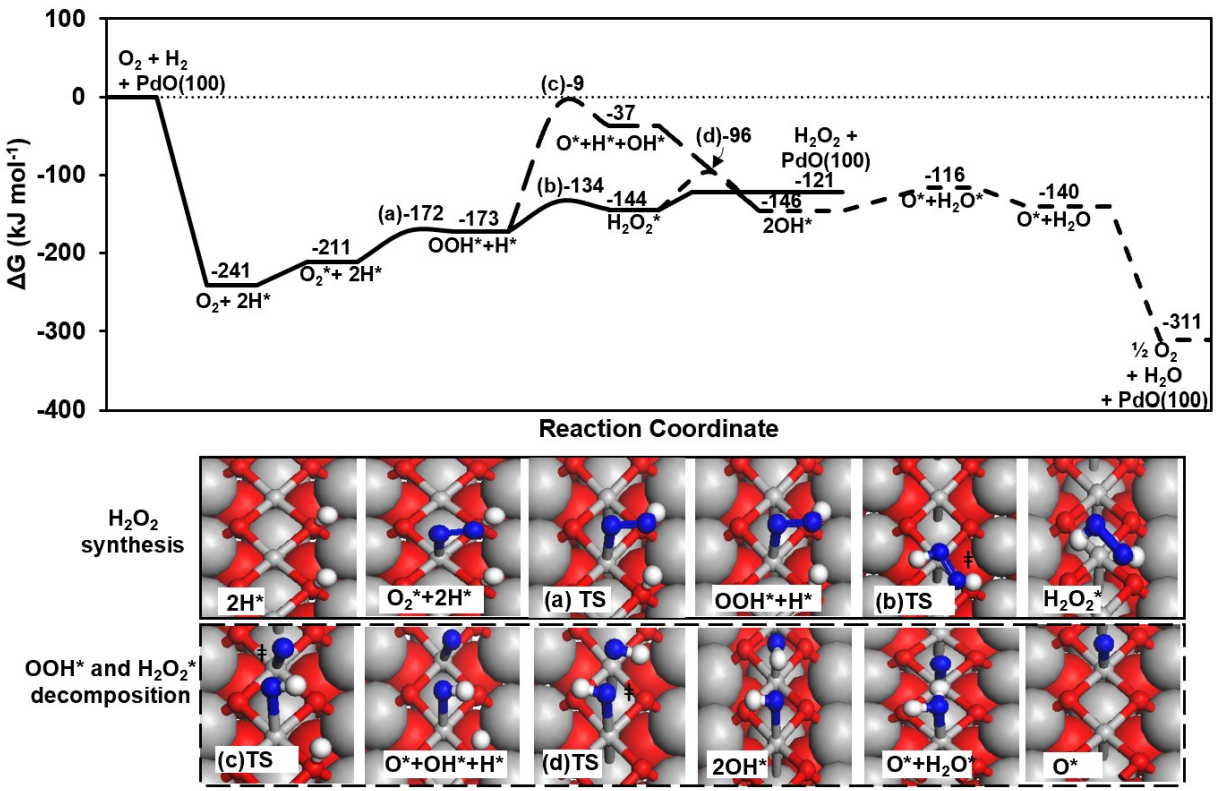

Figure 5. DFT-derived free energies (300 K; 1 bar) of intermediates and TSs involved in H_2O_2 synthesis and decomposition elementary steps (in Scheme 1) on PdO(100); the free energies of O_2 and H_2 and PdO(100) are taken as reference. Electronic energies (without any corrections) are shown in Figure S32 as a reference.

The above results already illustrate the contrast between PdO(101) and PdO(100); O-O cleavage in OOH* faces a higher free energy barrier on PdO(100) than on PdO(101) (164 vs. 11 kJ mol^{-1}). Moreover, on PdO(100), H_2O_2*, once formed, faces a lower free energy barrier to desorb H_2O_2 as a product (+23 kJ mol^{-1}) than to cleave its O-O bond to form two OH* ($\Delta G^{\ddagger}_{300K}$ = 48 kJ mol^{-1}). We suggest that OOH* and H_2O_2* decomposition is limited on PdO(100) due to the perturbation of coordinatively saturated Pd_{4c} sites by O_{3c} atoms, resulting in the preference of O-H formation over O-O cleavage steps. As particle size decreases, $Pd_{13}O_{18}$, which contains coordinatively saturated Pd_{4c} atoms, becomes the relevant model. This cluster has high barriers for O-O cleavage in both OOH* and H_2O_2* ($\Delta G^{\ddagger}_{300K}$ = 229 and 99 kJ mol^{-1}, respectively), exhibiting a trend similar to that on PdO(100); the electronic and free energy diagrams for the $Pd_{13}O_{18}$ cluster model are shown in Figure S33.

Up to this point, we have shown that the decomposition of the OOH* intermediate and/or the H_2O_2* product is thermodynamically and kinetically favorable on systems with Pd-Pd ensemble sites such as metallic Pd and PdO(101) surfaces. As these Pd-Pd sites are perturbed by O-atoms as in Pd_5O_4/Pd(111) and PdO(100) surfaces, the barriers for these decomposition steps become higher, which suggests their ability

to prevent the decomposition of OOH* and H_2O_2* and promote the selectivity and yield of H_2O_2. A rigorous analysis of primary H_2O_2 selectivity, however, requires a quantitative assessment of H_2O_2 formation rates (via the reduction of OOH*; step 4 in Scheme 1) and OOH* decomposition rates (via the O-O cleavage in OOH*; step 6 in Scheme 1) on each Pd, PdO/Pd, and PdO model, which will be discussed next.

3.2. Effects of Pd- and O- coordination in Pd, PdO/Pd, and PdO structures on their primary H_2O_2 selectivity

The primary H_2O_2 selectivity depends on the kinetic preference of OOH* to selectively form H_2O_2* via its reaction with H* without cleaving its O-O bond (steps 4 and 6 in Scheme 1):[16,17,77]

$$The\ primary\ H_2O_2\ selectivity = \frac{rate\ of\ step\ 4}{rate\ of\ step\ 6} = \frac{k_{O-H}[H*][OOH*]}{k_{O-O}[*][OOH*]}, \quad (16)$$

where [OOH*], [H*], and [*] reflect the respective surface coverages of OOH*, H*, and empty * sites. The rate constant for step 4 ($k_{O\text{-}H}$) depends on the free energy of the O-H formation TS ($G^{\ddagger}_{O-H}$), referenced to the OOH* and H* precursors (G_{OOH^*} and G_{H^*}):

$$k_{O-H} = \frac{N_A RT}{h}\exp\left(-\frac{\Delta G^{\ddagger}_{O-H}}{RT}\right) = \frac{N_A RT}{h}\exp\left[-\frac{\left(G^{\ddagger}_{O-H} - G_{OOH^*} - G_{H^*}\right)}{RT}\right] \quad (17)$$

where N_A is Avogadro's number, R is the gas constant, and h is Planck's constant. The rate constant for O-O cleavage in OOH* ($k_{O\text{-}O}$) reflects the free energy of the O-O cleavage TS ($G^{\ddagger}_{O-O}$) referenced to the OOH* and * precursors (G_{OOH^*} and G_*):

$$k_{O-O} = \frac{N_A RT}{h}\exp\left(-\frac{\Delta G^{\ddagger}_{O-O}}{RT}\right) = \frac{N_A RT}{h}\exp\left[-\frac{\left(G^{\ddagger}_{O-O'} - G_{OOH^*} - G_*\right)}{RT}\right] \quad (18)$$

Equation 18 then can be rewritten as:

$$The\ primary\ H_2O_2\ selectivity = \frac{rate\ of\ step\ 4}{rate\ of\ step\ 6} = \exp\left[-\frac{\left(\Delta G^{\ddagger}_{O-O} - \Delta G^{\ddagger}_{O-H}\right)}{RT}\right]\frac{[H*]}{[*]} \quad (19)$$

Figures 6a and 6b show the electronic energy components of $\Delta G^{\ddagger}_{O-H}$ and $\Delta G^{\ddagger}_{O-O}$ barriers ($\Delta E^{\ddagger}_{O-H}$ and $\Delta E^{\ddagger}_{O-O}$) and calculated $k_{O\text{-}H}/k_{O\text{-}O}$ ratios (from free energy barriers via Eqns. 17 and 18) for all Pd, PdO/Pd, and PdO models shown in Figure 1.

Recall that the Pd-H bond in H* and the Pd-O bond in OOH* weakens as H* is transferred to the O-atom in OOH* (step 4; Scheme 1) to form H_2O_2*. On metallic Pd models, the O-H bond formation step (ΔE_{O-H}) becomes thermodynamically less favorable in the order of Pd(111) > Pd(100) > Pd_{55} > Pd_{13} (black symbols in Fig. 6a), reflecting the systems with lower CN Pd atoms that bind OOH* and H* species more strongly. Specifically, the adsorption energies of OOH* become more negative as the average CN decreases in the Pd models (-126 > -186 > -192 > -212 kJ mol^{-1} for Pd(111), Pd(100), Pd_{55}, and Pd_{13}; Table 1). Similarly, H* adsorption also becomes stronger in this order (-381~-370 > -388 > -419 kJ mol^{-1} for

Pd(111)~Pd(100), Pd_{55}, and Pd_{13}; Table 1). Consequently, the activation barrier ($\Delta E^{\ddagger}_{O-H}$) increases for the systems as the average CN in Pd models decreases, following the trend expected from the Brønsted−Evans−Polanyi (BEP) relationship.[78]

In contrast, the Pd-O bonds in O* and OH* are formed as the O-O bond in OOH* is cleaved in the O-O cleavage step (step 6; Scheme 1). The thermodynamic favorability of ΔE_{O-O} follows the order of Pd(111) < Pd(100) < Pd_{55} < Pd_{13} (Fig. 6b). The observed trend again reflects the presence of lower CN Pd atoms in the smaller cluster models, which bind OH* adsorbates more strongly. As Pd particle size decreases from Pd(111) to Pd_{55} to Pd_{13}, the OH* adsorption energy becomes more negative (-260 to -294 to and -326 kJ mol^{-1}; Table 1), rendering the O-O bond cleavage step thermodynamically more favorable on smaller particles. The O* adsorption energy, while varying less dramatically, also becomes more negative as Pd particle size decreases (-441 to -456 kJ mol^{-1} for Pd(111) and Pd(100), and -469 to -493 kJ mol^{-1} for Pd_{13} and Pd_{55}; Table 1). The activation barriers for this O-O cleavage step ($\Delta E^{\ddagger}_{O-O}$), however, remain essentially zero on all metallic Pd models (black symbols in Fig. 6b) as the reaction energy changes from -222 to -140 kJ mol^{-1} due to the very exothermic nature of this step. This trend is consistent with the Hammond's postulate,[79] which predicts that very exothermic reactions involve early TSs that resemble energies and structures of the reactant states and thus their activation barriers are less sensitive to the reaction energies.

DFT-derived $\Delta G^{\ddagger}_{O-H}$ and $\Delta G^{\ddagger}_{O-O}$ values (after ZPVE and thermal corrections) lead to k_{O-H}/k_{O-O} ratios that are larger for Pd surfaces with larger Pd CN (Pd(111)> Pd(100) ~ Pd_{55} > Pd_{13}; Fig. 6c), indicating an improvement in the primary H_2O_2 selectivity for larger Pd nanoparticles. Similar to our conclusion, Wilson and coworkers[14] also suggested that the selectivity can be improved by utilizing larger Pd nanoparticles. However, the reasoning to reach such a conclusion was different; they reported that the measured enthalpic barriers for the O-H formation step remained similar as the average Pd diameter decreased from 7 to 0.7 nm, while that for O-O cleavage in OOH* decreased from 32 to 18 kJ mol^{-1}. Regardless of this trend, these k_{O-H}/k_{O-O} values have remained smaller than unity on all metallic Pd models (10^{-10}-10^{-4}; 300 K; Fig. 6c), indicating poor primary H_2O_2 selectivities of metallic Pd irrespective of exposed facets and particle sizes.

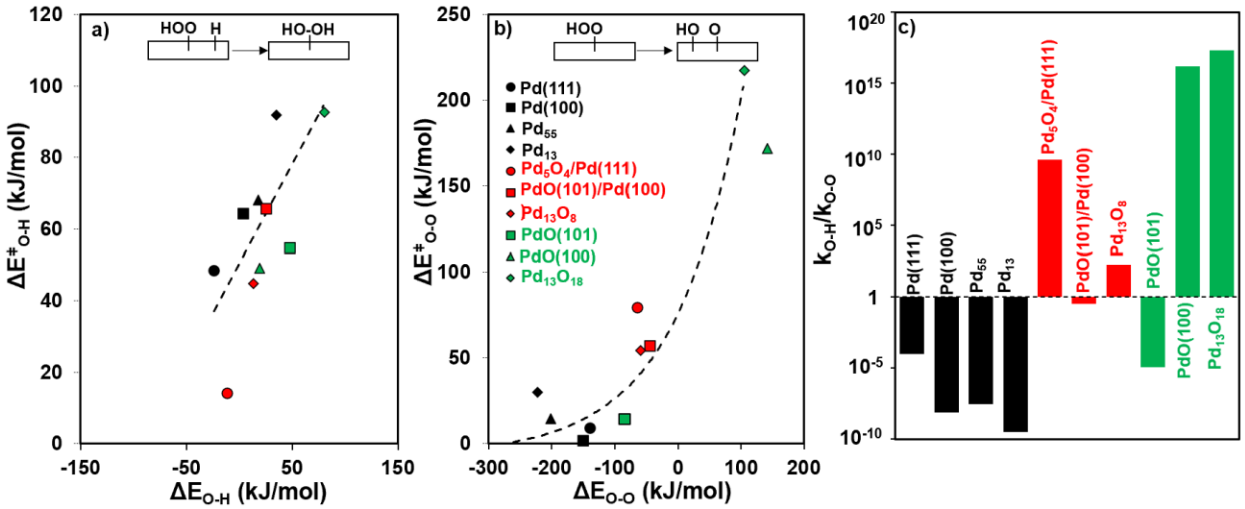

Figure 6. DFT-derived activation energies as a function of respective reaction energies for a) step 4 and b) step 6 in Scheme 1. Dashed lines represent the trend, and black, red, and green colors represent clean metals, surface oxides, and bulk oxides, respectively. c) Estimated $k_{O\text{-}H}/k_{O\text{-}O}$ ratio (via Eqn. 19). DFT-derived structures of involved intermediates and TSs are shown in Section S4 (SI) for metallic Pd models and in Figures 7 and 8 for surface oxide and bulk oxide models.

Table 1. DFT-derived adsorption energies (kJ mol^{-1}) of the most stable configuration of intermediates on Pd, PdO/Pd, and PdO slab and cluster models.[a]

	O*	H*	OH*	OOH*	H_2O_2*
Pd(111)	-456	-381	-260	-126	-67
Pd(100)	-441	-370	-294	-186	-79
Pd_{55}	-493	-388	-294	-192	-71
Pd_{13}	-469	-419	-326	-212	-99
Pd_5O_4/Pd(111)	-314	-364	-223	-124	-68
PdO(101)/Pd(100)	-339	-383	-256	-155	-67
$Pd_{13}O_8$	-286	-405	-205	-113	-68
PdO(101)	-375	-395	-304	-239	-118
PdO(100)	-170	-448	-154	-101	-70
$Pd_{13}O_{18}$	-207	-503	-167	-89	-65

[a]These energies reflect electronic energies without any corrections, referenced to the energies of corresponding adsorbates in the gas phase and the clean catalyst model.

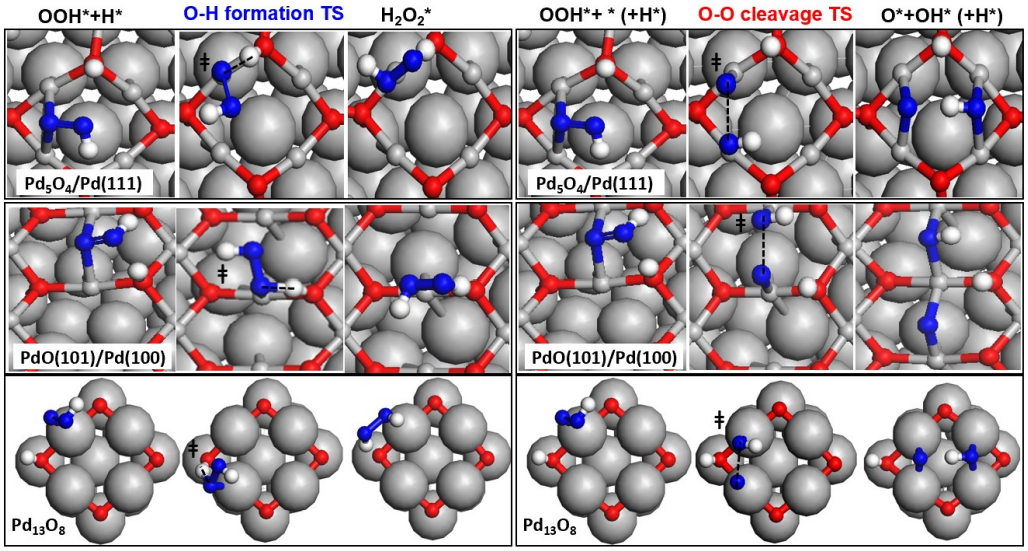

Figure 7. DFT-derived structures of intermediates and TSs involved in the O-H bond formation step (step 4; Scheme 1) and the O-O cleavage step (step 6; Scheme 1) on surface oxide models (in Fig. 1). Grey atoms are Pd, red atoms are surface O*, blue atoms are O in intermediates and TSs, and white atoms are H.

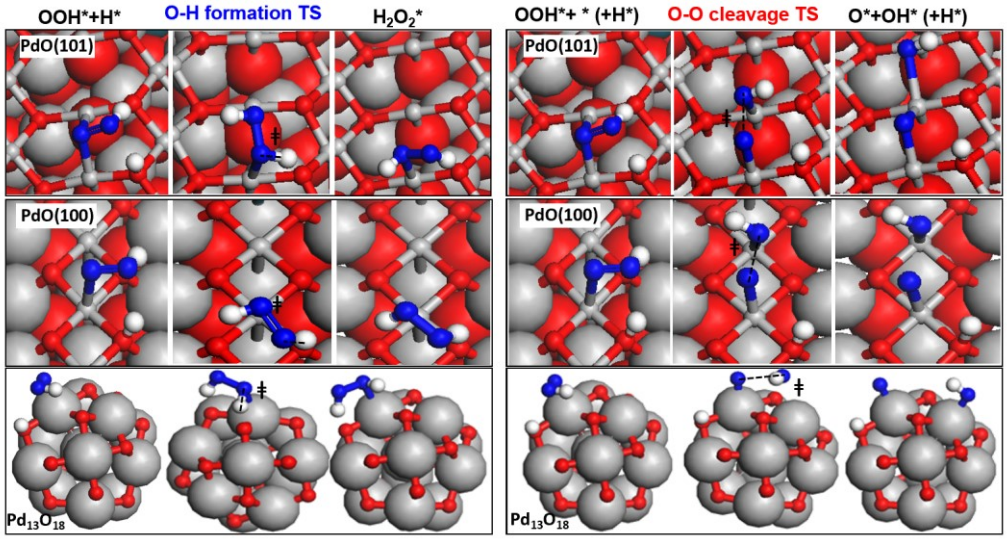

Figure 8. DFT-derived structures of intermediates and TSs involved in the O-H bond formation step (step 4; Scheme 1) and the O-O cleavage step (step 6; Scheme 1) on bulk oxide models (in Fig. 1). Grey atoms are Pd, red atoms are surface O*, blue atoms are O in intermediates and TSs, and white atoms are H.

The primary H_2O_2 selectivity changes when surface and bulk oxides form under suffuciently high oxdizing conditions. For instance, as Pd(111) oxidizes to form a surface oxide (Pd_5O_4/Pd(111) in Fig. 1), the $k_{O\text{-}H}/k_{O\text{-}O}$ ratio increases from 10^{-4} to 10^{9} (300 K; Fig. 6c), indicating a dramatic improvement in the primary H_2O_2 selectivity. Similarly, as Pd(100) forms a corresponding surface oxide (PdO(101)/Pd(100) in Fig. 1), the $k_{O\text{-}H}/k_{O\text{-}O}$ ratio increases from 10^{-9} to 10^{-1} (300 K; Fig. 6c). Yet, despite the dramatic improvement

in H_2O_2 selectivity, its value on PdO(101)/Pd(100) (10^{-1}; 300 K; Fig. 6c) is still smaller than unity, indicating that the O-O cleavage step is still favored over the O-H bond formation step.

The differences in H_2O_2 selectivity between Pd_5O_4/Pd(111) and PdO(101)/Pd(100) are reflective of their structural differences. Pd_5O_4 contains Pd_{2c} and O_{3c} pairs in a rectangle-like configuration (Pd_{2c}-Pd_{2c} = 0.281 - 0.299 nm) over a Pd(111) substrate (Fig. 1). The Pd_{2c}-$Pd_{substrate}$ distance ranges between 0.257 and 0.288 nm depending on the location of the P_{2c} atoms. PdO(101)/Pd(100) contains Pd_{2c} atoms connected to O_{3c} atoms (Pd_{2c}-Pd_{2c} = 0.305 nm) over a Pd(100) substrate, where the Pd_{2c}-$Pd_{substrate}$ ranges between 0.266 and 0.330 nm. Both surfaces also contain Pd_{4c} and O_{4c} atoms, but these sites are less reactive and all intermediates and TSs tend to bind on undercoordinated Pd_{2c} and O_{3c} (Fig. 7). Bader charge analysis demonstrates that the Pd_{2c} and O_{3c} atoms have similar charges on both surfaces (+0.49e and -0.76e on Pd_5O_4/Pd(111) and +0.47e and -0.75e on PdO(101)/Pd(100)). Yet, the Pd_{2c} and O_{3c} atoms in PdO(101)/Pd(100) bind all intermediate species more strongly than those in Pd_5O_4/Pd(111), as reflected in the more negative adsorption energies of O* (-339 vs. -314 kJ mol^{-1}), H* (-383 vs. -364 kJ mol^{-1}), OH* (-256 vs. -223 kJ mol^{-1}), and OOH* (-155 vs. -124 kJ mol^{-1}) as shown in Table 1.

The stronger adsorption of intermediates on PdO(101)/Pd(100), in turn, makes the O-H bond formation step (step 4; Scheme 1) thermodynamically and kinetically less favorable than on Pd_5O_4/Pd(111) (ΔE_{O-H} = +25 vs. -12 and $\Delta E^{\ddagger}_{O-H}$ = 66 vs. 14 kJ mol^{-1}; Fig. 6a). In contrast, the O-O bond cleavage step (step 6; Scheme 1) is thermodynamically less facile but kinetically more favorable on PdO(101)/Pd(100) than on Pd_5O_4/Pd(111) (ΔE_{O-O} = -45 vs. -65 kJ mol^{-1} and $\Delta E^{\ddagger}_{O-O}$ = 57 vs. 79 kJ mol^{-1}; Fig. 6b), which may be attributed to the different O*/OH* configurations on these surfaces. O* and OH* adsorb at neighboring bridge sites on PdO(101)/Pd(100). While O* and OH* also adsorb at bridge sites on Pd_5O_4/Pd(111), they further interact with each other via a hydrogen bond, making the product state more stable and thermodynamically favorable (Fig. 7). These trends in O-H formation and O-O cleavage steps lead to a k_{O-H}/k_{O-O} ratio of 10^{-1} vs. 10^{9} for PdO(101)/Pd(100) and Pd_5O_4/Pd(111), respectively (300 K; Fig. 6c). These dramatic differences in primary H_2O_2 selectivity between PdO(101)/Pd(100) and Pd_5O_4/Pd(111) indicate that the selectivity for H_2O_2* formation cannot be guaranteed by the formation of PdO/Pd, but that the oxide must additionally have an adequate surface structure.

As particle size decreases, $Pd_{13}O_8$, which has a surface oxide structure with Pd_{2c}-O_{3c} sites (Fig. 1), appears to be favored for the cluster with 13 Pd atoms over a range of O* chemical potentials (see Section 3.4). This oxide structure resembles that of Pd_5O_4/Pd(111) with a square-like configuration of Pd_{2c}-O_{3c} pairs (Pd_{2c}-Pd_{2c} = 0.294 nm). However, it differs in that it does not have any Pd_{4c} or O_{4c} sites and is "curved" nature due to the spherical shape of the cluster.

On $Pd_{13}O_8$, OOH* adsorbs atop of Pd_{2c} (Fig. 7), in contrast to adsorbing at a bridge site on Pd_5O_4/Pd(111) because the Pd_{2c}-Pd_{2c} distance is slightly larger on the cluster (0.294 vs. 0.281 nm). A

comparison of energies of different adsorbate binding modes on $Pd_{13}O_8$ can be found in Table S8. The Pd_{2c} atoms in $Pd_{13}O_8$ are weaker Lewis acids than those in Pd_5O_4/Pd(111), reflected by less negative adsorption energies of O* (-286 vs. -314 kJ mol^{-1}) , OH* (-205 vs. -223 kJ mol^{-1}), and OOH* (-113 vs. -124 kJ mol^{-1}), as shown in Table 1. In contrast, the O_{3c} atoms in $Pd_{13}O_8$ are stronger Lewis bases than those in Pd_5O_4/Pd(111), as shown by a more negative H* adsorption energy (-405 vs. -364 kJ mol^{-1}; Table 1). This strong H* binding compensates for the weaker OOH* binding on $Pd_{13}O_8$, leading to the O-H bond formation step (step 4; Scheme 1) that is kinetically and thermodynamically less favorable on $Pd_{13}O_8$ than on Pd_5O_4/Pd(111) (ΔE_{O-H} = 13 vs. -12 kJ mol^{-1}; $\Delta E^{\ddagger}_{O-H}$= 45 vs. 14 kJ mol^{-1}). O-O cleavage in OOH* is also thermodynamically more facile on Pd_5O_4/Pd(111) than on $Pd_{13}O_8$ (ΔE_{O-O} = -65 vs. -60 kJ mol^{-1}) although it is kinetically less facile on Pd_5O_4/Pd(111) ($\Delta E^{\ddagger}_{O-O}$= 79 vs. 54 kJ mol^{-1}). Correspondingly, the estimated primary H_2O_2 selectivity as given by the k_{O-H}/k_{O-O} ratio is 10^2 on $Pd_{13}O_8$, which is dramatically higher than on metallic Pd_{13} (10^{-10}; 300 K; Fig. 6c), but lower than on Pd_5O_4/Pd(111) (10^9; 300 K; Fig. 6c).

Bulk PdO models become relevant at very high oxidizing conditions. PdO(101) contains undercoordinated Pd_{3c} atoms (Fig. 1) on top of which, OOH* tends to cleave its O-O bond with a small activation barrier; such a barrier is smaller than that to reduce to OOH* to form H_2O_2* (14 vs. 55 kJ mol^{-1}; Figs. 6a-b). These barriers lead to an estimated k_{O-H}/k_{O-O} ratio much smaller than unity on PdO(101) (10^{-5}; 300 K; Fig. 6c). Hence the kinetic preference on PdO(101) is more akin to that on metallic Pd models (10^{-10} to 10^{-4}; 300 K; Fig. 6c), presumably due to the presence of undercoordinated Pd_{3c} ensemble sites that resemble those on metallic Pd.

The structure of bulk PdO(101) differs from the epitaxial PdO(101) layer on Pd(100) (PdO(101)/Pd(100)). The Pd_{3c} atom in PdO(101) interacts with three O-atoms, while Pd_{2c} in PdO(101)/Pd(100) interacts with two surface O-atoms as there are no O-atoms in the subsurface (Fig.1). These structural differences lead to very different charge distributions in Pd atoms; Pd_{3c} in PdO(101) is more positively charged than Pd_{2c} in PdO(101)/Pd(100) (+0.64e and +0.47e, respectively, from the Bader charge analysis). The more positively charged Pd_{3c} atoms in PdO(101) are thus stronger Lewis acids, reflected in more negative adsorption energies of O*(-375 vs. -339 kJ mol^{-1}), OH* (-304 vs. -256 kJ mol^{-1}), OOH* (-239 vs. -155 kJ mol^{-1}) and H_2O_2* (-118 vs. -67 kJ mol^{-1}) on such sites (Table 1). The O_{3c} atoms in these surfaces, however, have similar coordination environments; they are both coordinated to three Pd atoms. As a result, their charges are similar for both surfaces (-0.75e in both cases), rendering similar H* adsorption energies on these sites (-395 vs. -383 kJ mol^{-1}; Table 1). While the O-H formation step is thermodynamically less favorable on PdO(101) than PdO(101)/Pd(100) (ΔE_{O-H} = +47 vs. +25 kJ mol^{-1}), DFT calculations suggest that this step is kinetically more favorable on PdO(101) ($\Delta E^{\ddagger}_{O-H}$ = 55 vs. 66 kJ mol^{-1}; Fig. 6a). O-O cleavage in OOH*, however, is thermodynamically and kinetically more favorable on PdO(101) with stronger Lewis acid sites than on PdO(101)/Pd(100) (ΔE_{O-O} = -84 vs. -45 kJ mol^{-1}; $\Delta E^{\ddagger}_{O-O}$ =

14 vs. 57 kJ mol^{-1}; Fig. 6b). These barriers lead to the estimated k_{O-H}/k_{O-O} ratio that is smaller on PdO(101) than on PdO(101)/Pd(100) (10^{-5} vs. 10^{-1}; 300 K; Fig. 6c). Yet, in both cases, the k_{O-H}/k_{O-O} ratio is smaller than unity indicating a lack of H_2O_2 selectivity stemming from the presence of undercoordinated Pd_{3c} and Pd_{2c} atoms.

The primary H_2O_2 selectivity estimated by the k_{O-H}/k_{O-O} ratio is much larger than unity on PdO(100) (10^{16}; 300 K; Fig. 6c), which features the fully coordinated Pd_{4c} sites. This is in stark contrast to the k_{O-H}/k_{O-O} ratio of 10^{-5} on PdO(101) that has undercoordinated Pd_{3c} sites. The estimated k_{O-H}/k_{O-O} ratio is also larger than unity (10^{17}, 300 K; Fig. 6c) on the $Pd_{13}O_{18}$ cluster, which also contains surface Pd_{4c} atoms in 4-fold coordination. In this $Pd_{13}O_{18}$ cluster, which results from full oxidation of the Pd_{13} cluster, O-atoms are in either 2- or 3-fold coordination (O_{2c}, O_{3c}; Fig. 1). H atoms tend to bind more strongly on O_{2c} than on O_{3c} as reflected by the more negative H* adsorption energy (-503 vs. -466 kJ mol^{-1}; Table S11). Note that the O-H formation step is thermodynamically and kinetically more favorable on PdO(100) than on $Pd_{13}O_{18}$ (ΔE_{O-H} = 19 vs. 81 kJ mol^{-1}; $\Delta E^{\ddagger}_{O-H}$ = 49 vs. 93 kJ mol^{-1}; Fig. 6a). This trend reflects the O_{3c} atom in PdO(100) that binds H* less strongly than the O_{2c} atom in $Pd_{13}O_{18}$ (-448 vs. -503 kJ mol^{-1}; Table 1), making it easier to transfer that H* to OOH*. Although OOH* adsorbs in an atop configuration on Pd_{4c} sites in both PdO(100) and $Pd_{13}O_{18}$, OOH* adsorption is slightly more favorable on PdO(100) than on $Pd_{13}O_{18}$ (-101 vs. -89 kJ mol^{-1}; Table 1). The O-O cleavage step is thermodynamically less favorable on PdO(100) than on $Pd_{13}O_{18}$ (ΔE_{O-O} = 142 vs. 106 kJ mol^{-1}; Fig. 6b) because of the strong binding nature of OOH* as the reactant and the weaker binding of O* and OH* products on PdO(100). Yet, DFT calculations suggest that such a step is kinetically more favorable on PdO(100) than on $Pd_{13}O_{18}$ ($\Delta E^{\ddagger}_{O-O}$ = 172 vs. 217 kJ mol^{-1}; Fig. 6a). This trend reflects the "curved" nature of the $Pd_{13}O_{18}$ cluster that causes the O-O cleavage TS to only weakly interact with the neighboring Pd_{4c} site as opposed to interacting with two Pd_{4c} sites on PdO(100) (Fig. 8), even though the "straight" Pd_{4c}-Pd_{4c} distance is longer in PdO(100) than in $Pd_{13}O_{18}$ (0.305 nm and 0.280 nm, respectively). Regardless, estimated k_{O-H}/k_{O-O} ratios are much larger than unity on both PdO(100) and $Pd_{13}O_{18}$ models (10^{16} and 10^{17}, 300 K; Fig. 6c), reflecting very high primary H_2O_2 selectivities.

In summary, DFT-derived k_{O-H}/k_{O-O} ratios are smaller than unity for all metallic Pd models (10^{-10}-10^{-4}; 300 K; Fig. 6c), indicating very low primary H_2O_2 selectivities on metallic Pd regardless of particle size. As Pd starts to oxidize, O-atoms start to perturb Pd-Pd ensemble sites and the possibility of observing a preference for O-H bond formation over cleavage of the O-O bond in OOH* arises. However, whether O-H bond formation is actually preferred in a given oxidized system or not depends on the coordination environment of Pd-O sites, surface structure, and charge density. In the smallest Pd clusters (~0.5 nm), oxidation seemed to consistently engender environments that favored O-H bond formation over O-O cleavage. However in some surface models, O-O cleavage was preferred, particularly in those still retaining Pd-Pd ensembles in their structure despite oxidation (e.g., PdO(101) and PdO(101)/Pd(100)). As these

surface models are usually considered representative of the facets that show up on larger particles (> 5 nm in diameter), the observations in this section suggest that as the Pd particle size increases, the positive effect of oxidation on H_2O_2 primary selectivity may be hindered by the presence of "O-O cleavage-friendly" facets where Pd-Pd ensembles have not been fully disrupted. Resulting design principles may even translate to other systems such as Pd-Au catalysts, where high H_2O_2 selectivities have been reported,[16] due to the disturbance of Pd-Pd ensemble sites by Au atoms.[81] Such scenarios also invite careful study of the structure of Pd-Au surfaces at operando conditions during H_2O_2 synthesis, as H_2O_2 selectivities are highly sensitive to the Pd coordination environment.

3.3. DFT assessments of H_2O_2 decomposition pathways on Pd, PdO/Pd and PdO catalysts

While the previous section focused on primary H_2O_2 selectivity (the tendency to form H_2O_2* from OOH* via O-H formation), it must be recognized that a catalyst with high primary H_2O_2 selectivity could still result in low H_2O_2 yield if H_2O_2* formed easily decomposes. Such a decomposition involves O-O bond cleavage in H_2O_2* to form 2OH* (step 12 in Scheme 1), which leads to the formation of H_2O and O_2 products (steps 7-11 in Scheme 1). In this section, the H_2O_2 decomposition step is studied to assess whether catalysts with high primary H_2O_2 selectivities can maintain high H_2O_2 yields by imposing high barriers in H_2O_2 decomposition pathways.

Figure 9a shows DFT-derived activation barriers for cleaving the O-O bond in H_2O_2* ($\Delta E^{\ddagger}_{O-O',H_2O_2*}$; step 12 in Scheme 1) as a function of the corresponding reaction energies ($\Delta E_{O-O',H_2O_2*}$). We find O-O cleavage in H_2O_2* to be very exothermic on all metallic Pd models, ranging between -270 and -206 kJ mol^{-1} (black symbols in Fig. 9a). The thermodynamic favorability follows the order of Pd(111) < Pd(100) < Pd_{55} < Pd_{13}, similar to the previously discussed trend for O-O cleavage in OOH* (which was controlled by the presence of less coordinated Pd atoms). As this step is very exothermic on all metallic Pd models, the barriers remain nearly zero (2-15 kJ mol^{-1}; Fig. 9a) in these systems. Thus, not only is H_2O_2* formation is difficult on metallic Pd, but any formed H_2O_2* also easily decomposes, indicating a direct correlation between primary H_2O_2 selectivity and H_2O_2* product "stability".

Similar to how O-O cleavage of OOH* tends to become more difficult as Pd oxidizes, O-O cleavage in H_2O_2* also tends to become thermodynamically and kinetically less favorable upon Pd oxidation. The reaction energies ($\Delta E_{O-O',H_2O_2*}$) on PdO/Pd slab models (Pd_5O_4/Pd(111) and PdO(101)/Pd(100)), which are relevant to surface oxides formed on large particles (> 5nm), are -153 and -133 kJ mol^{-1}, respectively, which are less favorable than the -206 to -270 kJ/mol range observed on metallic Pd models (Fig. 9a). Accordingly, the H_2O_2* decomposition barriers for these surface oxide models ($\Delta E^{\ddagger}_{O-O',H_2O_2*}$ = 26 kJ mol^{-1} on both surfaces; Fig. 9a) are larger compared to those on metallic Pd surfaces (2-18 kJ mol^{-1} range; Fig.

9a). As large Pd nanoparticles completely turn into bulk PdO, the barriers become even larger on facets that feature fully coordinated Pd- and O-atoms. Specifically, $\Delta E^{\ddagger}_{O-O',H_2O_2*}$ is 65 kJ/mol on PdO(100) as the fully coordinated Pd_{4c} atoms bind the O-O cleavage TS more weakly than the H_2O_2* precursor. Yet, on PdO(101), which features Pd ensembles of more metallic, undercoordinated Pd atoms (Pd_{3c}-Pd_{3c} sites), the barrier is very similar to those on the metallic Pd systems ($\Delta E^{\ddagger}_{O-O',H_2O_2*}$ = 12 kJ mol^{-1} vs. 2-18 kJ mol^{-1}, respectively).

On the other hand, as noted in the previous section, these Pd_{3c}-Pd_{3c} or Pd_{2c}-Pd_{2c} ensemble sites are not present on the $Pd_{13}O_{18}$ cluster model. The O-O cleavage reaction energies on these clusters becomes increasingly unfavorable as Pd_{13} oxidizes ($\Delta E_{O-O',H_2O_2*}$= -270 to -133 to -6 kJ mol^{-1} on Pd_{13}, $Pd_{13}O_8$, and $Pd_{13}O_{18}$, respectively; Fig. 9a). Accordingly, the barrier for H_2O_2* decomposition increases from 6 kJ mol^{-1} on Pd_{13} to 35 kJ mol^{-1} on $Pd_{13}O_8$ and to 108 kJ mol^{-1} on $Pd_{13}O_{18}$ (Fig. 9a). This demonstrates a noticeable increase in activation barrier as O* atoms are incorporated into the Pd_{13} structure, making it more difficult to cleave the O-O bond in H_2O_2*. Additionally, it is worth noting that this O-O cleavage step becomes even more difficult as particle size decreases; the barriers on $Pd_{13}O_{18}$ and PdO(100) are 108 vs. 65 kJ mol^{-1}, respectively (Fig. 9a), even though the reaction energies were similar (-6 vs. -2 kJ mol^{-1}). On $Pd_{13}O_{18}$, the O-O cleavage TS in H_2O_2* is similar in configuration to the O-O cleavage TS in OOH*, where the "curved" nature of the cluster lowers the stability of the TS relative to the initial state (Fig. S33), increasing its activation barrier in comparison to PdO(100), its larger counterpart.

Given the similarity between the OOH* cleavage and H_2O_2 decomposition steps (steps 6 and 12 in Scheme 1), it is perhaps not surprising that the same reasons that explain trends in O-O cleavage in OOH* cleavage also explain O-O cleavage in H_2O_2*. This is further reflected in the linear correlation between the barriers for these two steps (Fig. 9b). The existence of this correlation suggests that Pd/PdO surfaces that decompose H_2O_2 significantly would also *tend to* exhibit low primary H_2O_2 selectivity in the direct synthesis process, and vice versa. This observation supports the use of H_2O_2 decomposition as a descriptor of H_2O_2 selectivity as it has been done in the literature.[12,24] However, one should be careful in correlating measured H_2O_2 decomposition rates and kinetic trends to understand H_2O_2 selectivities in the synthesis process. The state of the catalyst during H_2O_2 synthesis and decomposition may differ significantly, and as discussed so far, not only the oxidation state of Pd but also its coordination environment can have a significant impact on the favorability of competing reaction pathways. Partly motivated by this fact, we now proceed to discuss the most thermodynamically relevant states of Pd under O_2, H_2O_2/H_2O, and O_2/H_2 environments on the basis of *ab initio* thermodynamics.

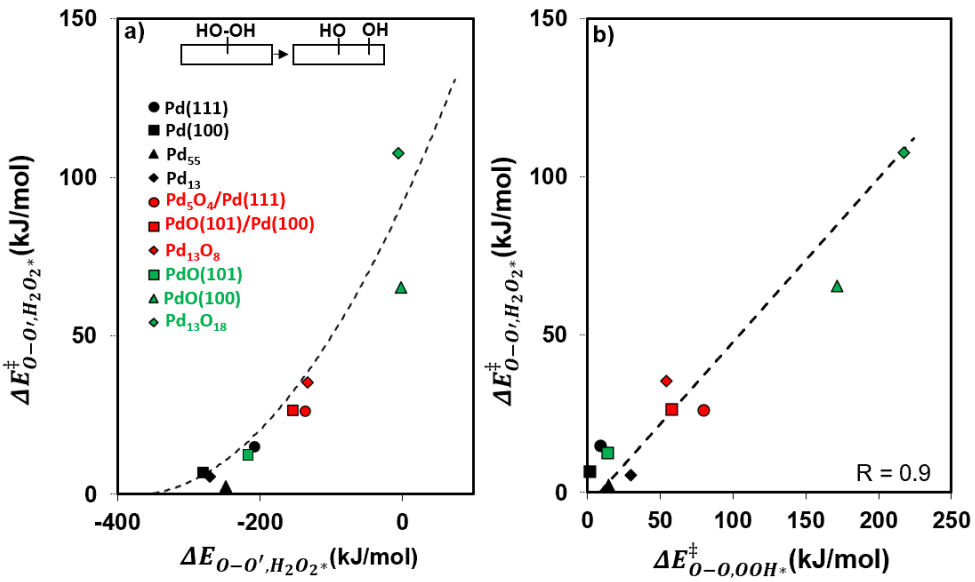

Figure 9. (a) DFT-derived activation energies for cleaving the O-O bond in H_2O_2* (step 12 in Scheme 1) as a function of respective reaction energies and b) DFT-derived activation energies for cleaving the O-O bond in H_2O_2*($\Delta E^{\ddagger}_{O-O',H2O2*}$) vs. OOH* ($\Delta E^{\ddagger}_{O-O,OOH*}$). DFT-derived structures of intermediates and TSs involved in the O-O cleavage step (in H_2O_2* to form two OH*) on each surface can be found in Section S4.

3.4. Pd to PdO phase transformation in O_2, H_2O_2/H_2O, and O_2/H_2 environments

The thermodynamics of Pd oxidation in an O_2 environment has been widely studied in literature both experimentally[40,42,45] and theoretically.[40,44,80] Yet, to the best of our knowledge, previous theory-driven phase diagrams have only focused on slab models of Pd(100)[45] and Pd(111)[40] and a cluster model (~3 nm) comprised of (111), (100), and (110) facets,[63] leaving a knowledge gap in understanding the particle size effects in Pd oxidation process. Moreover, thermodynamics of Pd oxidation in H_2O_2 environment has not been discussed before, which is important given that both the oxidation state of Pd and its coordination environment impact H_2O_2 synthesis and decomposition kinetics. Results in previous sections showed that H_2O_2 can easily decompose on metallic Pd systems to form O* and H_2O* via steps that are nearly barrierless. The relevant barriers for H_2O_2 decomposition on all metallic Pd models (via O-O cleavage in H_2O_2*, 2 – 15 kJ mol^{-1}) are even smaller than those for O_2 activation (via O-O cleavage in O_2* , 34 – 54 kJ mol^{-1}; Fig. S35). Since O_2 activation on metallic Pd has previously been shown to occur even at very low temperatures (≤ 200 K),[74,81] the smaller barriers for H_2O_2 decomposition suggest it can also occur at low temperatures on metallic Pd, oxidizing it to form a surface or bulk oxide.

Figure 10a shows the change in the grand potential (normalized by surface area; Δφ; Eq.4) upon Pd(111) oxidation as a function of the O* chemical potential (μ_{O*}, referenced to O_2; Eq. 11) at a fixed temperature of 300 K. At low μ_{O*} values, Pd(111) prefers to remain clean. As μ_{O*} increases, Pd(111) prefers to feature a 0.25 O* monolayer (ML; the ratio of O* to surface Pd atoms), then to feature a surface oxide

layer (Pd_5O_4/Pd(111)) as μ_{O*} continues to increase, before fully turning into bulk PdO when μ_{O*} is sufficiently high. Note that the maximum O* surface coverage on Pd(111) before forming a surface oxide is limited to 0.25 ML because the repulsive interactions among bound O* species become too strong beyond this coverage, consistent with trends in previous reports.[40,44,82] Such a trend is also reflected in DFT-derived O* adsorption energies that become less favorable above 0.25 ML, as shown in Figure S36. For Pd(100), the thermodynamically most stable phase changes from Pd(100) to PdO(101)/Pd(100), and then to bulk PdO as μ_{O*} increases (Fig. S11a); the O* covered Pd(100) surfaces do not appear as the most stable phases even after including Pd(100) models with a wide range of O* coverages (0.0625 –1 ML).

For the Pd_{13} cluster model, the most stable phase changes from Pd_{13}, to $Pd_{13}O_8$ and finally to $Pd_{13}O_{18}$ upon the increase in μ_{O*} (Fig. S11b). Note that in contrast to O* adsorption on Pd(111) that is limited to 0.25 ML, the average O* adsorption energy on Pd_{13} does not vary up to 0.67 ML (corresponding to the $Pd_{13}O_8$ cluster), after which point the repulsion between O* starts to affect the O* adsorption energy (Fig. S36). Such a trend reflects how repulsions between neighboring O* species are alleviated by the curved nature of the Pd_{13} cluster and the ability of small clusters to modify Pd-Pd bond distances to accommodate more O* atoms; the average Pd-Pd bond distance in Pd_{13} is ~0.28 nm, while $Pd_{13}O_{18}$ exhibits longer Pd-Pd distances (0.29 – 0.35 nm). A similar phenomena was observed by Loveless *et al.*, who demonstrated that the curved Ru_{201} cluster model can accommodate CO molecules up to 1.55 CO* coverages, which was limited to 0.75 ML on the flat Ru(0001) slab model.[83]

The μ_{O*} values can be related to O_2 pressure and temperature via Equation 11, as shown in Figures 10b-d for the Pd(111), Pd(100), and Pd_{13} oxidation processes. For example, at 900 K, Pd(111) becomes covered with 0.25 ML O* ($P_{O2} \geq 10^{-5}$ bar) and forms a surface oxide (Pd_5O_4/Pd(111)) ($P_{O2} \geq 10^{-3}$ bar), before converting into bulk PdO once the O_2 pressure reaches 10 bar. Similarly, at 900 K, Pd(100) forms PdO(101)/Pd(100) at 10^{-5} bar O_2 before transforming to bulk PdO at 10 bar O_2. These trends on Pd slab models agree quantitatively with previous theoretical studies.[40,44]

Indicative of size effects, the small Pd_{13} clusters seem to oxidize more easily, with Pd_{13} turning into $Pd_{13}O_8$ ($O/Pd_s = 0.67$) at lower O_2 pressure (10^{-12} bar), compared to 10^{-3} and 10^{-5} bar O_2 required to form surface oxides on Pd(111) and Pd(100). These results are consistent with O_2 uptake experiments on Pd/Al_2O_3, which demonstrated a downshift in the O_2 pressure needed to oxidize Pd to PdO (from 0.8 bar to 0.2 bar at 973 K) as the size of the original metallic Pd particles decreased from 8.8 to 1.8 nm.[27] This trend, in turn, is a consequence of the stronger O* binding observed in smaller Pd particles, as shown by more negative O* adsorption energies for Pd_{13} clusters compared to those for Pd(111) and Pd(100) (-146 vs. -129 and -119 kJ mol^{-1}, respectively, at low O* coverage limits < 0.1 ML, referenced to ½ O_2(g); Fig. S36). Yet, the formation of $Pd_{13}O_{18}$ ($O/Pd_s = 1.5$) occurs at 10^3 bar of O_2 pressure, which is even higher than that required to form bulk PdO from Pd(111) and Pd(100) surfaces (10 bar O_2; 900 K). The small Pd clusters

thus tend to present at "surface oxides" at a wider O_2 pressure range, although for such small clusters, the differentiation of bulk and surface becomes less relevant.

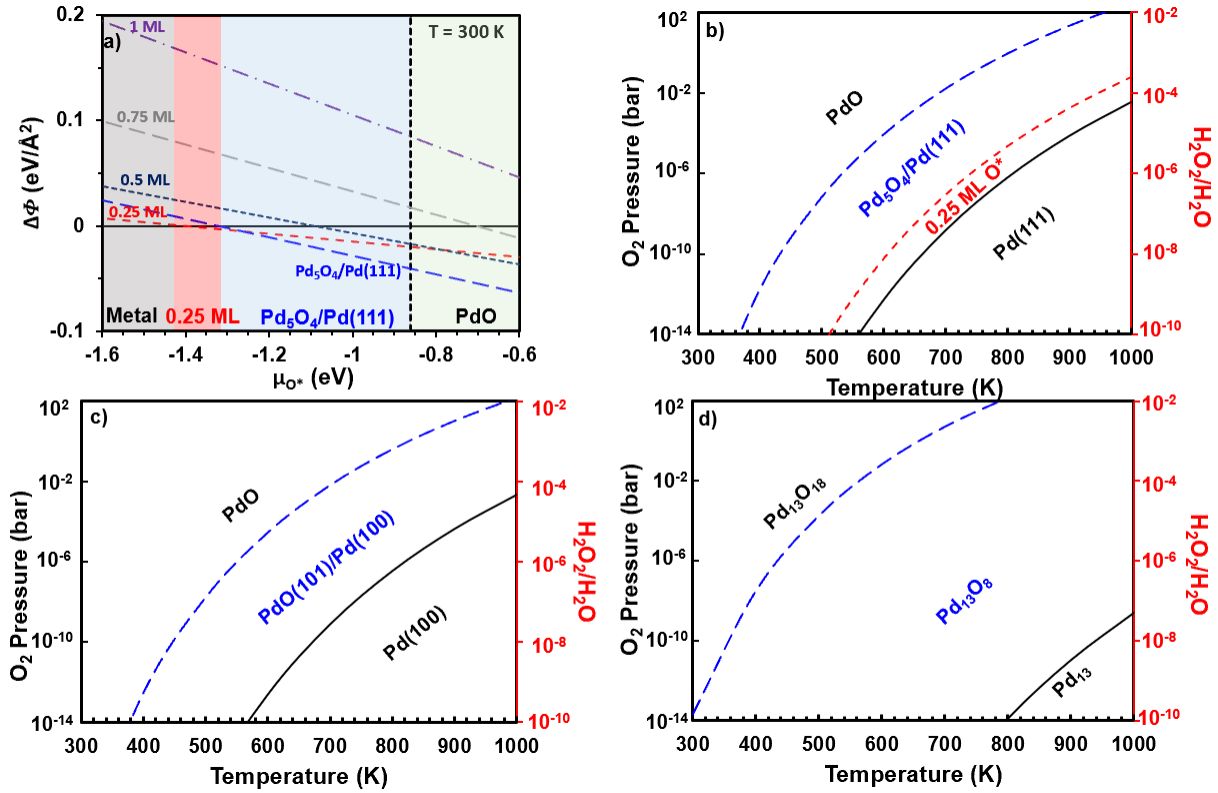

Figure 10. The change in the grand potential (normalized by surface area; Δφ; Eq.4) upon Pd(111) oxidation as a function of the O* chemical potential (μ_{O*}, referenced to O_2; Eq. 11) at 300 K. Similar plots for other models (Pd(100) and Pd_{13}) can be found in Figure S11 (SI). The panels b-d represent the thermodynamically most stable-structures of b) Pd(111), c) Pd(100), and d) Pd_{13} at a range of temperatures (300-1000K), O_2 pressures (bar), and H_2O_2/H_2O ratios.

Alternatively, one can instead relate μ_{O*} to a pressure ratio of H_2O_2 and H_2O, and to a temperature via Equation 12. For instance, at 900 K, Pd(111) transforms to 0.25 ML O*, P_5O_4/Pd(111), and to PdO at H_2O_2/H_2O pressure ratios of 10^{-6}, 10^{-5}, and 10^{-3} (Fig. 10b). Pd(100) transforms to PdO(101)/Pd(100) and PdO at H_2O_2/H_2O pressure ratios of 10^{-6} and 10^{-3} (Fig. 10c). As particle size decreases, Pd_{13} transforms to $Pd_{13}O_8$ and $Pd_{13}O_{18}$ at H_2O_2/H_2O pressure ratios of 10^{-9} and 10^{-1} (at 900 K; Fig. 10d). During typical H_2O_2 decomposition experiments, H_2O_2/H_2O ratios range between 0.08 to 0.6 M H_2O_2 in H_2O (corresponding to H_2O_2/H_2O ratios of 10^{-3}-10^{-2}) at 307 K,[12] indicating that PdO would be the relevant state of the catalyst for Pd surfaces and smaller Pd_{13} clusters according to our DFT-derived phase diagrams (Figs. 10b-d).

It should be noted that while qualitative agreements can be expected between theoretical phase diagrams and experimental observations, sources of quantitative discrepancies may stem from DFT errors in estimating the interaction strength between O and Pd atoms, but also from the assumption of thermodynamic equilibration. While the latter assumption could largely hold true at high enough

temperatures to overcome all kinetic hurdles, bulk oxidation can be limited by the dissolution of surface-bound O* into the bulk at lower temperatures. Thus, the formation of metastable structures that differ from those predicted from thermodynamics may occur at lower temperatures.[40,45] For instance, a surface phase diagram for Pd(100) obtained using in-situ surface X-ray diffraction (SXRD) (10^{-10}- 1bar O_2; 300-1000 K) detected PdO(101)/Pd(100) even at 1 bar O_2 and 600 K, [45] the condition at which PdO is expected to be thermodynamically most stable (Fig. 10b). This result reflects that at lower temperatures (T ≤ 600 K), a kinetic hinderance may prevent surface oxides from transforming to bulk oxides. In contrast, the smaller Pd particles are less likely to be impacted by such O* diffusion limitations, allowing them to oxidize to PdO/Pd or PdO at lower O_2 pressures or H_2O_2/H_2O ratios. Nonetheless, the results presented here should be safely interpreted as indicative of relative thermodynamic driving forces to form an oxide phase.

Finally, during H_2O_2 synthesis, the relevant Pd, PdO/Pd, and PdO states depend not only on the oxidant pressures (O_2), but also on the reductant pressures (H_2). The phase diagrams for Pd(111) in O_2 and H_2 mixtures are shown in Figure S13 (SI), which agree quantitatively with those reported previously.[20] These results, in turn, show that at typical H_2O_2 synthesis conditions (5-100 bar O_2 and H_2; 275-315 K), β-PdH(111)and Pd_5O_4/Pd(111) would be the active phases of the catalyst at low and high O_2/H_2 ratios, respectively. These conclusions are consistent with in-situ XAS studies by Adams et al. who detected surface oxides in O_2-rich condition (0.6 bar H_2, 10 bar O_2, 298K; in H_2O) and β-PdH_x in H_2-rich condition (7 bar H_2, 0.6 bar O_2, 298K; in H_2O).[23] Although the further exploration of these hydride phases is beyond the scope of this work, this exercise highlights that the active Pd phase is highly sensitive to reaction conditions. It is also worth noting that Pd-based catalysts have also been explored for alkane oxidation using O_2 and H_2 mixtures to form H_2O_2 in-situ.[6,84] Our phase diagram at moderate conditions for C_3H_8 oxidation catalysis (10^{-3}-1 bar O_2 and H_2; 450 K)[85] suggests Pd_5O_4/Pd(111) to be the relevant state during these reactions. These results, in turn, show the importance of the Pd oxidation states and their surface structures on reaction kinetics and selectivities, requiring a careful characterization of the catalyst at relevant conditions to provide detailed structure-function relationships in catalysis.

4. Conclusion

This study used DFT treatments and *ab initio* thermodynamics to explore particle size effects on the thermodynamics of Pd to PdO phase transformation and its consequences on H_2O_2 synthesis and decomposition pathways. Primary H_2O_2 selectivities are governed by the kinetic preference of OOH* species to either react with H* to form H_2O_2* or to decompose into O* and OH* that ultimately leads to the formation of undesired H_2O and O_2 products. This kinetic preference is estimated for metallic Pd, surface oxides, and bulk PdO models based on the ratio of rate constants for these two elementary steps

($k_{O\text{-}H}/k_{O\text{-}O}$). While $k_{O\text{-}H}/k_{O\text{-}O}$ increased in the order of Pd_{13} < Pd_{55} ~ Pd(100) < Pd(111) indicating the improved primary selectivity for larger Pd particles, it still remained smaller than unity on all metallic Pd models (10^{-10}-10^{-4}; 300 K), indicating that O-O cleavage in OOH* is kinetically preferred over O-H formation regardless of exposed facet or particle size.

At higher chemical potentials of oxygen, metallic Pd oxidizes into surface and bulk oxides. As Pd atoms are perturbed by O* atoms, the primary H_2O_2 selectivity significantly improves; at 300 K, the $k_{O\text{-}H}/k_{OO}$ ratio increases from 10^{-4} to 10^{9} and to 10^{16} as Pd(111) oxidizes to Pd_5O_4/Pd(111) and to PdO(100). Consistently, the $k_{O\text{-}H}/k_{OO}$ ratio increases from 10^{-10} to 10^{2} and to 10^{17} (at 300 K) as the small Pd_{13} nanocluster oxidizes into $Pd_{13}O_8$ and into $Pd_{13}O_{18}$. However, such selectivity enhancements are not observed for surface and bulk oxides that persistently contain rows of undercoordinated Pd-Pd ensemble sites, such as PdO(101)/Pd(100) and PdO(101). These surface structures are absent in smaller Pd nanoparticles, indicating that these smaller clusters can be more selective in H_2O_2 synthesis when they are oxidized. These trends of primary H_2O_2 selectivities match those observed for H_2O_2 decomposition rates via O-O bond cleavage, indicating that the catalysts with high primary H_2O_2 selectivity are also resistive to H_2O_2 decomposition.

Ab-initio thermodynamic calculations are used to probe the relevant phase of Pd during H_2O_2 synthesis and decomposition reactions. These results demonstrated that in comparison to larger Pd surfaces, smaller Pd particles tend to form surface oxides at lower O* chemical potential (and thus at lower O_2 pressures or H_2O_2/H_2O ratios). These small Pd_{13} clusters also present as surface oxides at a larger range of O*chemical potentials. Our DFT-derived phase diagrams suggest that large Pd surfaces and small Pd particles will form bulk oxides under typical H_2O_2 decomposition reactions, although the formation of bulk oxides of large Pd particles may be kinetically hindered by O* diffusions at low temperatures. In contrast, Pd surfaces can present as a surface oxide or β-PdH_x under typical H_2O_2 synthesis or alkane oxidation conditions. Considering the significant impacts of oxidation states and surface structures on H_2O_2 selectivities and yields, these results urges careful consideration in correlating measured H_2O_2 decomposition rates and kinetic trends to understanding H_2O_2 selectivities in the synthesis process.

Acknowledgements

We thank Emily Volk, Michelle Nolen, and Benjamin Appleby (Colorado School of Mines) for providing careful proofreading of the manuscript. S.K. acknowledges financial support from Colorado School of Mines (startup funding). D.A.G-.G. acknowledges financial support from the National Science Foundation through grant CBET-1921484. This research used resources from the Colorado School of Mines supercomputing center (http://ciarc.mines.edu/hpc) and the National Energy Research Scientific Computing Center, a DOE Office of Science User Facility supported by the Office of Science of the U.S.

Department of Energy under Contract No. DE-AC02-05CH11231 using NERSC award BES-ERCAP0021167.

References

(1) Lewis, R. J.; Hutchings, G. J. Recent Advances in the Direct Synthesis of H_2O_2. ChemCatChem 2019, 11 (1), 298–308. https://doi.org/10.1002/CCTC.201801435.

(2) Flaherty, D. W. Direct Synthesis of H_2O_2 from H_2 and O_2 on Pd Catalysts: Current Understanding, Outstanding Questions, and Research Needs. ACS Catal 2018, 8 (2), 1520–1527. https://doi.org/10.1021/acscatal.7b04107

(3) Ranganathan, S.; Sieber, V. Recent Advances in the Direct Synthesis of Hydrogen Peroxide Using Chemical Catalysis—A Review. Catalysts 2018, 8 (9), 379. https://doi.org/10.3390/catal8090379.

(4) Menegazzo, F.; Signoretto, M.; Ghedini, E.; Strukul, G. Looking for the "Dream Catalyst" for Hydrogen Peroxide Production from Hydrogen and Oxygen. Catalysts 2019, 9 (3). https://doi.org/10.3390/catal9030251.

(5) Yu, X.; Moses, J. I.; Blecic, J.; Harrington, J.; Bowman, O.; Wilson, G. E.; Seymour, I. D.; Cavallaro, A.; Ruscic, B.; Pinzon, R. E.; von Laszewski, G.; Kodeboyina, D.; Burcat, A.; Leahy, D.; Montoya, D.; Wagner, A. F. Active Thermochemical Tables: Thermochemistry for the 21st Century. J Phys Conf Ser 2005, 16 (1), 561. https://doi.org/10.1088/1742-6596/16/1/078.

(6) Ab Rahim, M. H.; Forde, M. M.; Jenkins, R. L.; Hammond, C.; He, Q.; Dimitratos, N.; Lopez-Sanchez, J. A.; Carley, A. F.; Taylor, S. H.; Willock, D. J.; Murphy, D. M.; Kiely, C. J.; Hutchings, G. J. Oxidation of Methane to Methanol with Hydrogen Peroxide Using Supported Gold–Palladium Alloy Nanoparticles. Angewandte Chemie International Edition 2013, 52 (4), 1280–1284. https://doi.org/10.1002/ANIE.201207717.

(7) Petrov, A. W.; Ferri, D.; Krumeich, F.; Nachtegaal, M.; van Bokhoven, J. A.; Kröcher, O. Stable Complete Methane Oxidation over Palladium Based Zeolite Catalysts. Nat Commun 2018, 9 (1). https://doi.org/10.1038/s41467-018-04748-x

(8) Lewis, R. J.; Hutchings, G. J. Recent Advances in the Direct Synthesis of H2O2. ChemCatChem 2019, 11 (1), 298–308. https://doi.org/10.1002/CCTC.201801435.

(9) Danov, S. M.; Fedosov, A. E.; Lunin, A. v. Liquid-Phase Oxidation of Normal C10–C13 Hydrocarbons with Hydrogen Peroxide on the Titanium-Containing Catalyst TS-1: The Effect of Process Conditions on Product Composition. Catalysis in Industry 2010 2:3 2010, 2 (3), 239–245. https://doi.org/10.1134/S2070050410030062.

(10) Klemm, E.; Dietzsch, E.; Schwarz, T.; Kruppa, T.; Lange De Oliveira, A.; Becker, F.; Markowz, G.; Schirrmeister, S.; Ru, |; 1tte, S.; Caspary, K. J.; Schu, F.; Ho, D. Direct Gas-Phase Epoxidation of Propene with Hydrogen Peroxide on TS-1 Zeolite in a Microstructured Reactor. 2008. https://doi.org/10.1021/IE071343.

(11) Voloshin, Y.; Manganaro, J.; Lawal, A. Kinetics and Mechanism of Decomposition of Hydrogen Peroxide over Pd/SiO_2 Catalyst. Ind Eng Chem Res 2008, 47 (21), 8119–8125. https://doi.org/10.1021/ie8000452.

(12) Plauck, A.; Stangland, E. E.; Dumesic, J. A.; Mavrikakis, M. Active Sites and Mechanisms for H_2O_2 Decomposition over Pd Catalysts. Proc Natl Acad Sci U S A 2016, 113 (14), E1973–E1982. https://doi.org/10.1073/pnas.1602172113.

(13) Choudhary, V. R.; Samanta, C.; Choudhary, T. v. Factors Influencing Decomposition of H_2O_2 over Supported Pd Catalyst in Aqueous Medium. J Mol Catal A Chem 2006, 260 (1–2), 115–120. https://doi.org/10.1016/J.MOLCATA.2006.07.009.

(14) Wilson, N. M.; Flaherty, D. W. Mechanism for the Direct Synthesis of H_2O_2 on Pd Clusters: Heterolytic Reaction Pathways at the Liquid-Solid Interface. J Am Chem Soc 2016, 138 (2), 574–586. https://doi.org/10.1021/jacs.5b10669

(15) Wang, F.; Xia, C.; de Visser, S. P.; Wang, Y. How Does the Oxidation State of Palladium Surfaces Affect the Reactivity and Selectivity of Direct Synthesis of Hydrogen Peroxide from Hydrogen and Oxygen Gases? A Density Functional Study. J Am Chem Soc 2019, 141 (2), 901–910. https://doi.org/10.1021/jacs.8b10281

(16) Ricciardulli, T.; Gorthy, S.; Adams, J. S.; Thompson, C.; Karim, A. M.; Neurock, M.; Flaherty, D. W. Effect of Pd Coordination and Isolation on the Catalytic Reduction of O_2 to H_2O_2 over PdAu Bimetallic Nanoparticles. J Am Chem Soc 2021, 143 (14), 5445–5464. https://doi.org/10.1021/jacs.1c00539

(17) Wilson, N. M.; Priyadarshini, P.; Kunz, S.; Flaherty, D. W. Direct Synthesis of H_2O_2 on Pd and AuxPd1 Clusters: Understanding the Effects of Alloying Pd with Au. J Catal 2018, 357, 163–175. https://doi.org/10.1016/J.JCAT.2017.10.028.

(18) Beletskaya, A. v.; Pichugina, D. A.; Shestakov, A. F.; Kuz'Menko, N. E. Formation of H_2O_2 on Au_{20} and Au_{19} Pd Clusters: Understanding the Structure Effect on the Atomic Level. Journal of Physical Chemistry A 2013, 117 (31), 6817–6826. https://doi.org/10.1021/jp4040437.

(19) Yang, N.; Liu, J.; Sun, Y.; Zhu, Y. Au@PdOx with a PdOx-Rich Shell and Au-Rich Core Embedded in Co3O4 Nanorods for Catalytic Combustion of Methane. Nanoscale 2017, 9 (6), 2123–2128. https://doi.org/10.1039/c6nr08700k.

(20) Chen, L.; Medlin, J. W.; Grönbeck, H. On the Reaction Mechanism of Direct H_2O_2 Formation over Pd Catalysts. ACS Catal 2021, 11 (5), 2735–2745. https://doi.org/10.1021/acscatal.0c05548

(21) Ouyang, L.; Tian, P. F.; Da, G. J.; Xu, X. C.; Ao, C.; Chen, T. Y.; Si, R.; Xu, J.; Han, Y. F. The Origin of Active Sites for Direct Synthesis of H_2O_2 on Pd/TiO_2 Catalysts: Interfaces of Pd and PdO Domains. J Catal 2015, 321, 70–80. https://doi.org/10.1016/j.jcat.2014.10.003.

(22) Kanungo, S.; van Haandel, L.; Hensen, E. J. M.; Schouten, J. C.; Neira d'Angelo, M. F. Direct Synthesis of H2O2 in AuPd Coated Micro Channels: An in-Situ X-Ray Absorption Spectroscopic Study. J Catal 2019, 370, 200–209. https://doi.org/10.1016/J.JCAT.2018.12.017.

(23) Adams, J. S.; Chemburkar, A.; Priyadarshini, P.; Ricciardulli, T.; Lu, Y.; Maliekkal, V.; Sampath, A.; Winikoff, S.; Karim, A. M.; Neurock, M.; Flaherty, D. W. Solvent Molecules Form Surface Redox Mediators in Situ and Cocatalyze O_2 reduction on Pd. Science 2021, 371 (6529), 626–632. https://doi.org/10.1126/science.abc1339

(24) Gaikwad, A. G.; Sansare, S. D.; Choudhary, V. R. Direct Oxidation of Hydrogen to Hydrogen Peroxide over Pd-Containing Fluorinated or Sulfated Al_2O_3, ZrO_2, CeO_2, ThO_2, Y_2O_3 and Ga_2O_3 Catalysts

in Stirred Slurry Reactor at Ambient Conditions. J Mol Catal A Chem 2002, 181 (1–2), 143–149. https://doi.org/10.1016/S1381-1169(01)00359-4.

(25) Tian, P.; Ouyang, L.; Xu, X.; Ao, C.; Xu, X.; Si, R.; Shen, X.; Lin, M.; Xu, J.; Han, Y. F. The Origin of Palladium Particle Size Effects in the Direct Synthesis of H_2O_2: Is Smaller Better? J Catal 2017, 349, 30–40. https://doi.org/10.1016/J.JCAT.2016.12.004.

(26) Kim, S.; Lee, D. W.; Lee, K. Y.; Cho, E. A. Effect of Pd Particle Size on the Direct Synthesis of Hydrogen Peroxide from Hydrogen and Oxygen over Pd Core-Porous SiO_2 Shell Catalysts. Catal Letters 2014, 144 (5), 905–911. https://doi.org/10.1007/s10562-014-1235-3

(27) Chin, Y. H. C.; García-Diéguez, M.; Iglesia, E. Dynamics and Thermodynamics of Pd-PdO Phase Transitions: Effects of Pd Cluster Size and Kinetic Implications for Catalytic Methane Combustion. Journal of Physical Chemistry C 2016, 120 (3), 1446–1460. https://doi.org/10.1021/acs.jpcc.5b06677.

(28) Hafner, J. Ab-Initio Simulations of Materials Using VASP: Density-Functional Theory and Beyond. Journal of Computational Chemistry. John Wiley and Sons Inc. October 1, 2008, pp 2044–2078. https://doi.org/10.1002/jcc.21057.

(29) Blöchl, P. E. Projector Augmented-Wave Method. Phys Rev B 1994, 50 (24), 17953–17979. https://doi.org/10.1103/PhysRevB.50.17953.

(30) Perdew, J. P.; Burke, K.; Ernzerhof, M. Generalized Gradient Approximation Made Simple. Phys Rev Lett 1996, 77 (18), 3865. https://doi.org/10.1103/PhysRevLett.77.3865.

(31) Ropo, M.; Kokko, K.; Vitos, L. Assessing the Perdew-Burke-Ernzerhof Exchange-Correlation Density Functional Revised for Metallic Bulk and Surface Systems. Phys Rev B Condens Matter Mater Phys 2008, 77 (19), 195445. https://doi.org/10.1103/PhysRevB.77.195445

(32) Grimme, S. Semiempirical GGA-Type Density Functional Constructed with a Long-Range Dispersion Correction. J Comput Chem 2006, 27 (15), 1787–1799. https://doi.org/10.1002/jcc.20495.

(33) Monkhorst, H. J.; Pack, J. D. Special Points for Brillouin-Zone Integrations. Phys Rev B 1976, 13 (12), 5188. https://doi.org/10.1103/PhysRevB.13.5188.

(34) Froyen, S. Brillouin-Zone Integration by Fourier Quadrature: Special Points for Superlattice and Supercell Calculations. Phys Rev B 1989, 39 (5), 3168. https://doi.org/10.1103/PhysRevB.39.3168.

(35) Kan, H. H.; Colmyer, R. J.; Asthagiri, A.; Weaver, J. F. Adsorption of Water on a PdO(101) Thin Film: Evidence of an Adsorbed HO-H2O Complex. Journal of Physical Chemistry C 2009, 113 (4), 1495–1506. https://doi.org/10.1021/jp808008k

(36) Hakanoglu, C.; Hawkins, J. M.; Asthagiri, A.; Weaver, J. F. Strong Kinetic Isotope Effect in the Dissociative Chemisorption of H_2 on a PdO(101) Thin Film. Journal of Physical Chemistry C 2010, 114 (26), 11485–11497. https://doi.org/10.1021/jp101715j

(37) Dutta, B. N.; Dayal, B. Lattice Constants and Thermal Expansion of Palladium and Tungsten up to 878 °C by X-Ray Method. physica status solidi, 1963, 3 (12), 2253–2259. https://doi.org/10.1002/pssb.19630031207.

(38) Rogers, D. B.; Shannon, R. D.; Sleight, A. W.; Gillson, J. L. Crystal Chemistry of Metal Dioxides with Rutile-Related Structures. Inorg Chem 1969, 8 (4), 841–849. https://doi.org/10.1021/ic50074a029.

(39) Rogal, J.; Reuter, K.; Scheffler, M. Thermodynamic Stability of PdO Surfaces. Phys Rev B Condens Matter Mater Phys 2004, 69 (7), 075421. https://doi.org/10.1103/PhysRevB.69.075421.

(40) Klikovits, J.; Napetschnig, E.; Schmid, M.; Seriani, N.; Dubay, O.; Kresse, G.; Varga, P. Surface Oxides on Pd(111): STM and Density Functional Calculations. Phys Rev B Condens Matter Mater Phys 2007, 76 (4), 045405. https://doi.org/10.1103/PhysRevB.76.045405

(41) Todorova, M.; Lundgren, E.; Blum, V.; Mikkelsen, A.; Gray, S.; Gustafson, J.; Borg, M.; Rogal, J.; Reuter, K.; Andersen, J. N.; Scheffler, M. The Pd(100)–(5×5)R27°-O Surface Oxide Revisited. Surf Sci 2003, 541 (1–3), 101–112. https://doi.org/10.1016/S0039-6028(03)00873-2.

(42) Gabasch, H.; Unterberger, W.; Hayek, K.; Klötzer, B.; Kresse, G.; Klein, C.; Schmid, M.; Varga, P. Growth and Decay of the Pd(111)–Pd5O4 Surface Oxide: Pressure-Dependent Kinetics and Structural Aspects. Surf Sci 2006, 600 (1), 205–218. https://doi.org/10.1016/J.SUSC.2005.09.052.

(43) Kasper, N.; Nolte, ⊥ P; Stierle, A. Stability of Surface and Bulk Oxides on Pd(111) Revisited by in Situ X-Ray Diffraction. 2012. https://doi.org/10.1021/jp307434g.

(44) Todorova, M. Oxidation of Palladium Surfaces. Dissertation TU Berlin 2004, No. March, 1–124.

(45) Lundgren, E.; Gustafson, J.; Mikkelsen, A.; Andersen, J. N.; Stierle, A.; Dosch, H.; Todorova, M.; Rogal, J.; Reuter, K.; Scheffler, M. Kinetic Hindrance during the Initial Oxidation of Pd(100) at Ambient Pressures. Phys Rev Lett 2004, 92 (4), 4. https://doi.org/10.1103/PhysRevLett.92.046101.

(46) Wang, L.-L.; Johnson, D. D. Density Functional Study of Structural Trends for Late-Transition-Metal 13-Atom Clusters. Phys. Rev. B 2007 75, 235405 https://doi.org/10.1103/PhysRevB.75.235405.

(47) Efremenko, I.; Sheintuch, M. Quantum Chemical Study of Small Palladium Clusters. Surf Sci 1998, 414 (1–2), 148–158. https://doi.org/10.1016/S0039-6028(98)00508-1.

(48) Zhang, W.; Wang, L. Structure Effects on the Energetic, Electronic, and Magnetic Properties of Palladium Nanoparticles J. Chem. Phys 2003, 118, 5793. https://doi.org/10.1063/1.1557179.

(49) Xing, X.; Hermann, A.; Kuang, X.; Ju, M.; Lu, C.; Jin, Y.; Xia, X.; Maroulis, G. Insights into the Geometries, Electronic and Magnetic Properties of Neutral and Charged Palladium Clusters. Scientific Reports 2016, 6 (1), 1–11. https://doi.org/10.1038/srep19656.

(50) Rapps, T.; Ahlrichs, R.; Waldt, E.; Kappes, M. M.; Schooss, D.; Rapps, T.; Ahlrichs, R.; Waldt, E.; Kappes, M. M.; Schooss, D. On the Structures of 55-Atom Transition-Metal Clusters and Their Relationship to the Crystalline Bulk. Angewandte Chemie International Edition 2013, 52 (23), 6102–6105. https://doi.org/10.1002/ANIE.201302165.

(51) Doye, J. P. K.; Wales, D. J. Global Minima for Transition Metal Clusters Described by Sutton–Chen Potentials. New Journal of Chemistry 1998, 22 (7), 733–744. https://doi.org/10.1039/A709249K.

(52) Sheppard, D.; Terrell, R.; Henkelman, G. Optimization Methods for Finding Minimum Energy Paths. 2008. https://doi.org/10.1063/1.2841941.

(53) Henkelman, G.; Uberuaga, B. P.; Jó, H. A Climbing Image Nudged Elastic Band Method for Finding Saddle Points and Minimum Energy Paths. J Chem Phys 2000, 113 (22). https://doi.org/10.1063/1.1329672

(54) Henkelman, G.; Jónsson, H. A Dimer Method for Finding Saddle Points on High Dimensional Potential Surfaces Using Only First Derivatives. J Chem Phys 1999, 111 (15), 7010. https://doi.org/10.1063/1.480097.

(55) Tang, W.; Sanville, E.; Henkelman, G. A Grid-Based Bader Analysis Algorithm without Lattice Bias. J. Phys.: Condens. Matter 2009, 21, 84204–84211. https://doi.org/10.1088/0953-8984/21/8/084204.

(56) Frederiksen, T.; Paulsson, M.; Brandbyge, M.; Jauho, A. P. Inelastic Transport Theory from First Principles: Methodology and Application to Nanoscale Devices. Phys Rev B Condens Matter Mater Phys 2007, 75 (20), 205413. https://doi.org/10.1103/PhysRevB.75.205413

(57) McQuarrie, D. A. Statistical Mechanics. 2000, 641.

(58) Piccini, G.; Sauer, J. Effect of Anharmonicity on Adsorption Thermodynamics. J. Chem. Theory Comput. 2014, 10, 6, 2479–2487. https://doi.org/10.1021/ct500291x.

(59) Campbell, C. T.; Sellers, J. R. V. The Entropies of Adsorbed Molecules. J Am Chem Soc 2012, 134 (43), 18109–18115. https://doi.org/10.1021/ja3080117

(60) Plimpton, S. Fast Parallel Algorithms for Short-Range Molecular Dynamics. J Comput Phys 1995, 117 (1), 1–19. https://doi.org/10.1006/JCPH.1995.1039.

(61) Senftle, T. P.; Hong, S.; Islam, M. M.; Kylasa, S. B.; Zheng, Y.; Shin, Y. K.; Junkermeier, C.; Engel-Herbert, R.; Janik, M. J.; Aktulga, H. M.; Verstraelen, T.; Grama, A.; van Duin, A. C. T. The ReaxFF Reactive Force-Field: Development, Applications and Future Directions. Computational Materials. 2016, 2 (1), 1–14. https://doi.org/10.1038/npjcompumats.2015.11.

(62) Aktulga, H. M.; Fogarty, J. C.; Pandit, S. A.; Grama, A. Y. Parallel Reactive Molecular Dynamics: Numerical Methods and Algorithmic Techniques. Parallel Comput 2012, 38 (4–5), 245–259. https://doi.org/10.1016/J.PARCO.2011.08.005.

(63) Senftle, T. P.; Meyer, R. J.; Janik, M. J.; van Duin, A. C. T. Development of a ReaxFF Potential for Pd/O and Application to Palladium Oxide Formation. J Chem Phys 2013, 139 (4), 044109. https://doi.org/10.1063/1.4815820.

(64) Payne, M. C.; Teter, M. P.; Ailan, D. C.; Arias, T. A.; Joannopouios, J. D. Iterative Minimization Techniques for Ab Initio Total-Energy Calculations: Molecular Dynamics and Conjugate Gradients. 1992.

(65) Braga, C.; Travis, K. P. A Configurational Temperature Nosé-Hoover Thermostat. J Chem Phys 2005, 123 (13), 134101. https://doi.org/10.1063/1.2013227.

(66) Berendsen, H. J. C.; Postma, J. P. M.; van Gunsteren, W. F.; Dinola, A.; Haak, J. R. Molecular Dynamics with Coupling to an External Bath. J Chem Phys 1998, 81 (8), 3684. https://doi.org/10.1063/1.448118.

(67) Sholl, D. S.; Steckel, J. A. Density Functional Theory: A Practical Introduction. Density Functional Theory: A Practical Introduction 2009, 1–238. https://doi.org/10.1002/9780470447710.

(68) Reuter, K.; Scheffler, M. Composition and Structure of the RuO_2 110 Surface in an O_2 and CO Environment: Implications for the Catalytic Formation of CO_2. https://doi.org/10.1103/PhysRevB.68.045407.

(69) Chase, M. W. NIST-JANAF Thermochemical Tables, 4th Edition.

(70) Tanko, J. M. CRC Handbook of Chemistry and Physics: A Ready-Reference of Chemical and Physical Data, 85th Ed. J Am Chem Soc 2005, 127 (12), 4542–4542. https://doi.org/10.1021/ja041017a.

(71) Lunsford, J. H. The Direct Formation of H_2O_2 from H_2 and O_2 over Palladium Catalysts. Journal of Catalysis 2003, 216, 455–460. https://doi.org/10.1016/S0021-9517(02)00070-2.

(72) Tian, P.; Ouyang, L.; Xu, X.; Xu, J.; Han, Y. F. Density Functional Theory Study of Direct Synthesis of H_2O_2 from H_2 and O_2 on Pd(111), Pd(100), and Pd(110) Surfaces. Chinese Journal of Catalysis 2013, 34 (5), 1002–1012. https://doi.org/10.1016/S1872-2067(12)60537-3.

(73) Honkala, K.; Laasonen, K. Ab Initio Study of O_2 Precursor States on the Pd(111) Surface. J Chem Phys 2001, 115 (5), 2297. https://doi.org/10.1063/1.1384009.

(74) Montemore, M. M.; van Spronsen, M. A.; Madix, R. J.; Friend, C. M. O2 Activation by Metal Surfaces: Implications for Bonding and Reactivity on Heterogeneous Catalysts. Chem Rev 2018, 118 (5), 2816–2862. https://doi.org/10.1021/acs.chemrev.7b00217

(75) Cramer, C. J.; Tolman, W. B.; Theopold, K. H.; Rheingold, A. L. Variable Character of O - O and M - O Bonding in Side-on (H_2) 1:1 Metal Complexes of O_2. Proc Natl Acad Sci U S A 2003, 100 (7), 3635–3640. https://doi.org/10.1073/pnas.0535926100

(76) Li, H. C; Wan, Q.; Du, C.; Zhao, J.; Li, F.; Zhang, Y.; Zheng, Y.; Chen, M.; Zhang, K. H. L.; Huang, J.; Fu, G.; Lin, S.; Huang, X.; Xiong, H. Layered Pd Oxide on PdSn Nanowires for Boosting Direct H_2O_2 Synthesis. Nature Communications 2022, 13 (1), 1–10. https://doi.org/10.1038/s41467-022-33757-0.

(77) Li, J.; Ishihara, T.; Yoshizawa, K. Theoretical Revisit of the Direct Synthesis of H_2O_2 on Pd and Au@Pd Surfaces: A Comprehensive Mechanistic Study. Journal of Physical Chemistry C 2011, 115 (51), 25359–25367. https://doi.org/10.1021/jp208118e

(78) Cheng, J.; Hu, P.; Ellis, P.; French, S.; Kelly, G.; Lok, C. M. Brønsted-Evans-Polanyi Relation of Multistep Reactions and Volcano Curve in Heterogeneous Catalysis. Journal of Physical Chemistry C 2008, 112 (5), 1308–1311. https://doi.org/10.1021/jp711191j

(79) Hammond, G. S. A Correlation of Reaction Rates. J Am Chem Soc 1955, 77 (2), 334–338. https://doi.org/10.1021/ja01607a027

(80) Seriani, N.; Harl, J.; Mittendorfer, F.; Kresse, G. A First-Principles Study of Bulk Oxide Formation on Pd(100). Journal of Chemical Physics 2009, 131 (5), 054701. https://doi.org/10.1063/1.3187935.

(81) Rose, M. K.; Borg, A.; Dunphy, J. C.; Mitsui, T.; Ogletree, D. F.; Salmeron, M. Chemisorption of Atomic Oxygen on Pd(111) Studied by STM. Surf Sci 2004, 561 (1), 69–78. https://doi.org/10.1016/J.SUSC.2004.04.037.

(82) Zheng, G.; Altman, E. I. Oxidation of Pd(111). Surf Sci 2000, 462 (1), 151–168. https://doi.org/10.1016/S0039-6028(00)00599-9.

(83) Loveless, B. T.; Buda, C.; Neurock, M.; Iglesia, E. CO Chemisorption and Dissociation at High Coverages during CO Hydrogenation on Ru Catalysts. J Am Chem Soc 2013, 135 (16), 6107–6121. https://doi.org/10.1021/ja311848e

(84) Sajith, P. K.; Staykov, A.; Yoshida, M.; Shiota, Y.; Yoshizawa, K. Theoretical Study of the Direct Conversion of Methane to Methanol Using H_2O_2 as an Oxidant on Pd and Au/Pd Surfaces. Journal of Physical Chemistry C 2020, 124 (24), 13231–13239. https://doi.org/10.1021/ACS.JPCC.0C03237

(85) Bravo-Suárez, J. J.; Bando, K. K.; Akita, T.; Fujitani, T.; Fuhrer, T. J.; Oyama, S. T. Propane Reacts with O_2 and H_2 on Gold Supported TS-1 to Form Oxygenates with High Selectivity. Chemical Communications 2008, No. 28, 3272–3274. https://doi.org/10.1039/B800620B.